Winter 2020

Spatial and Temporal Occurrence of Preformed Nitrate Anomalies in the Subtropical Ocean

Adam Joseph Smyth
University of New Hampshire, Durham

SPATIAL AND TEMPORAL OCCURRENCE OF PREFORMED NITRATE ANOMALIES IN THE SUBTROPICAL OCEAN

By

ADAM J. SMYTH

THESIS

Submitted to the University of New Hampshire

in Partial Fulfillment of

the Requirements for the Degree of

Master of Science

in

Oceanography

December, 2020

This thesis was examined and approved in partial fulfillment of the requirements for the degree of Master of Science in Oceanography by:

Thesis Director, Dr. Robert T. Letscher,
Assistant Professor, Earth Sciences &
Ocean Process Analysis Laboratory (OPAL)

Dr. Kai Ziervogel, Research Assistant
Professor, Ocean Process Analysis Laboratory
(OPAL) & Earth Sciences

Dr. Thomas Lippman, Associate Professor,
Earth Sciences & Center for Coastal and
Ocean Mapping (CCOM)

On November 13th, 2020

Approval signatures are on file with the University of New Hampshire Graduate School.

ACKNOWLEDGEMENTS

This research was funded by a teaching assistantship from the University of New Hampshire's Earth Science department as well as a Summer Graduate Position in the University of New Hampshire's Institute of Earth, Oceans and Space (EOS).

These data were collected and made freely available by the International Argo Program and the national programs that contribute to it. (http://www.argo.ucsd.edu, http://argo.jcommops.org). The Argo Program is part of the Global Ocean Observing System. Argo (2000). Argo float data and metadata from Global Data Assembly Centre (Argo GDAC). SEANOE. http://doi.org/10.17882/42182

Special thanks to my family, friends, and colleagues for their support throughout the pursuit of this thesis.

TABLE OF CONTENTS

LIST OF TABLES

PAGE

LIST OF FIGURES

PAGE

ABSTRACT

Preformed nitrate ($PreNO_3$) was formulated to act as a conservative tracer of ocean circulation after accounting for the stoichiometry of marine biochemical reactions involving oxygen and nitrate. However, $PreNO_3$ anomalies have been identified within the shallow subtropical ocean, that describe the biological consumption or production of oxygen without assumed stoichiometric changes in nitrate, which still have yet to be fully explained. The mechanisms proposed to drive the formation of $PreNO_3$ anomalies are: vertically migrating phytoplankton (VMP), the export and subsequent remineralization of N-deficient transparent exopolymer particles (TEP, e.g. marine gels), and the remineralization of N-poor dissolved organic matter (DOM). Observations from the subtropical Pacific and Atlantic oceans taken by twenty Biogeochemical Argo (Bio-Argo) profiling floats which collectively span from 2007 to 2019 have been used to answer two questions related to $PreNO_3$ anomalies. What is the seasonality and geographic extents of subsurface negative $PreNO_3$ anomalies and euphotic zone positive $PreNO_3$ anomalies in the global subtropical ocean? What biogeochemical processes capable of generating $PreNO_3$ anomalies are consistent with the seasonality and spatial extents found in the Bio-Argo float records? Euphotic zone positive $PreNO_3$ anomalies are consistently observed between 30˚S and 50˚N, whereas subsurface negative $PreNO_3$ anomalies are absent in parts of the Equatorial West Pacific Ocean. The remineralization of N-poor DOM has been shown to contribute to $PreNO_3$ anomaly formation by previous studies and has been accounted for in this study. The geographic extents of the remaining $PreNO_3$ anomalies are consistent with previous observations of VMP taxa throughout the global subtropical ocean. The seasonal timing of euphotic zone positive $PreNO_3$ anomalies in relation to subsurface negative $PreNO_3$ anomalies indicates that both VMP and the export and remineralization of N-deficient TEP contribute to the formation of $PreNO_3$ anomalies. Since VMP include large diatoms that produce ballasted organic

matter while TEP may only sink slowly before remineralization, further investigation into the mechanisms generating PreNO_3 anomalies is needed to assess their roles in the future biological carbon pump in an expanding subtropical ocean ecosystem.

INTRODUCTION

$PreNO_3$ is a theoretically conservative tracer (Broecker 1974; Abell et al. 2005), derived to account for the stoichiometry of oxygen and nitrate in marine biological reactions and thus reveal spatial patterns of water mass mixing. $PreNO_3$ was derived to trace the mixing and circulation of deep water, since deep water produced in different parts of the ocean will have different $PreNO_3$ values (Broecker 1974). The calculation of $PreNO_3$ utilizes the well-known Redfield ratio to account for the O_2:N stoichiometry of biological reactions such as photosynthesis and respiration. $PreNO_3$ should be positive everywhere below the euphotic zone however, significant $PreNO_3$ anomalies (e.g. negative concentrations) have been identified within the subtropical ocean including the Hawaii Ocean Time Series (HOT) and the Bermuda Atlantic Time Series (BATS) (Emerson & Hayward, 1995; Johnson et al. 2010; Letscher & Villareal, 2018). The presence of these anomalies reveal biogeochemical processes operating with non-Redfield O_2:N stoichiometries describing biological consumption or production of oxygen without stoichiometric nitrate production or consumption, respectively. $PreNO_3$ anomalies highlight gaps in the current understanding of marine biogeochemical cycles of nitrogen, oxygen, and carbon in the ocean which oceanographers have been trying to explain for decades. The nitrogen and carbon cycle are tightly coupled (Gruber 2008) making filling the gaps in our understanding of the nitrogen cycle that much more important. This is especially true because atmospheric CO_2 concentrations are currently rising at an unprecedented rate as a result of anthropogenic perturbation. Additionally the subtropical ocean ecosystem is predicted to expand as a result of changes in climate (Polovina et al. 2008), which may result in the mechanism(s) driving the formation of subtropical $PreNO_3$ anomalies to play a greater role in ocean biogeochemistry into the future.

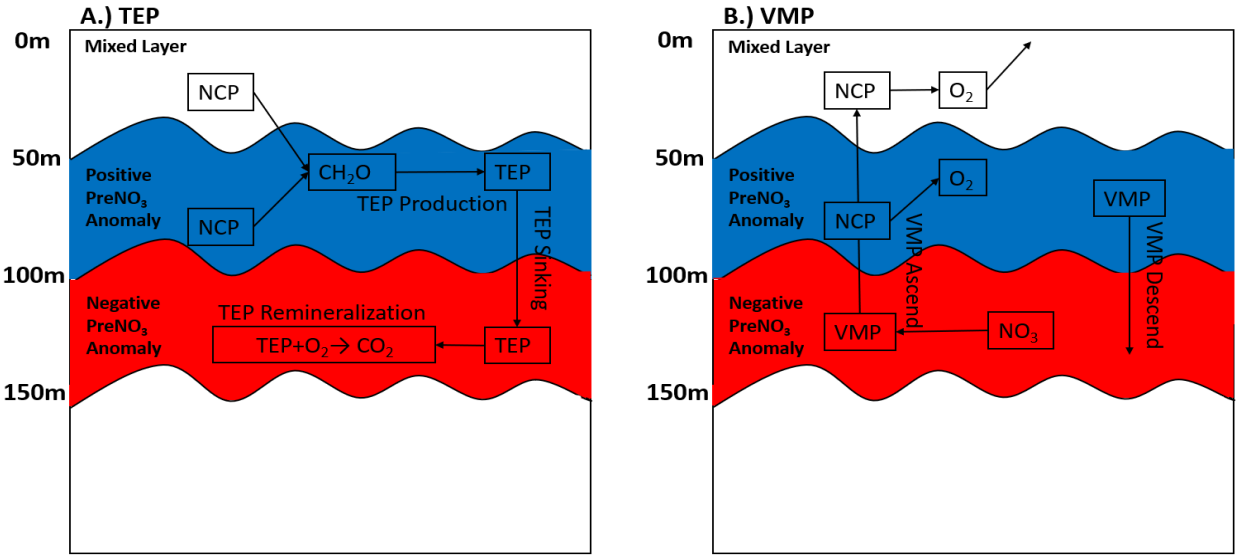

Figure 1. A.) TEP mechanism of euphotic zone positive $PreNO_3$ anomaly and sub-euphotic zone negative $PreNO_3$ anomaly formation diagram, depicting formation, sinking, and remineralization of TEP. B.) VMP mechanism euphotic zone positive $PreNO_3$ anomaly and sub-euphotic zone negative $PreNO_3$ anomaly formation diagram, depicting VMP descending, consuming NO_3 and ascending to photosynthesize.

Changes in dissolved nutrients and gases are linked by the stoichiometry of biochemical reactions. The stoichiometry of marine biochemical reactions typically follows the Redfield Ratio, 106 C: 16 N: 1P: 138 O_2 (Redfield et al. 1963). Negative $PreNO_3$ anomalies occur when there is oxygen consumption without stoichiometric nitrate production. Whereas positive $PreNO_3$ anomalies occur when there is oxygen production without the corresponding amount of nitrate consumption. There are three proposed mechanisms operating with non-Redfield stoichiometry to explain the formation of $PreNO_3$ anomalies: the export and sub euphotic zone remineralization of N-deficient DOM, Transparent Exopolymer Particles (TEP) export and sub-euphotic zone consumption, and Vertically Migrating Phytoplankton (VMP) utilizing sub euphotic zone stocks of nitrate to photosynthesize in the euphotic zone above (Johnson et al. 2010; Fawcett et al. 2018; Letscher & Villareal, 2018).

TEP are abiotically formed from the coagulation of carbohydrates with a high carbon to nitrogen ratio that are produced by phytoplankton and coagulate to form gel-like particles

(Alldredge et al. 1993; Wurl et al. 2011; Mari et al. 2017). As a marine gel, TEP can act as glue for marine snow aggregates and since TEP has a high carbon to nitrogen ratio it could prove significant to the biological carbon pump as an exporter of carbon to the seafloor (Passow 2002). TEP is positively buoyant when it is formed, but as TEP aggregates or becomes ballasted at the surface it eventually becomes negatively buoyant causing TEP to sink out of the euphotic zone (Wurl et al. 2011; Mari et al., 2017; Fawcett et al. 2018). Many vertical profiles of TEP show high concentrations closer to the surface with a decrease with depth, suggesting that TEP is produced shallower in the water column and is consumed at depth (Engel 2003; Wurl et al. 2011; Cisternas-Novoa et al. 2015). The extent to which bacteria degrade TEP is still not well understood and requires further investigation (Busch et al. 2017). Nutrient limitation stimulates the production of TEP, which is why TEP formation is more prevalent in the subtropical ocean (Myklestad 1995; Mari et al. 2017). It has been suggested that TEP production by phytoplankton can be increased by over 50% with an increase in temperature of 2˚C, due to enhanced extracellular release of DOM (Moran et al. 2006; Mari et al. 2017). The influence of temperature on TEP production as well as TEP's carbon rich composition both suggest that TEP could play a more significant role in the biological carbon pump with future ocean warming.

Another suggested mechanism is that phytoplankton could be consuming nitrate at depth and producing oxygen at the surface (Johnson et al. 2010; Letscher & Villareal, 2018). This is done by VMP, where phytoplankton travel down to the nitracline to consume nitrate and then ascend to the surface to photosynthesize (Villareal et al. 2014). Examples of taxa of phytoplankton which are known to vertically migrate are; *Pyrocystis, Ethmodiscus, Rhizosolenia* (Letscher & Villareal, 2018). The vertical migrating behavior of the VMP taxa; *Pyrocystis, Ethmodiscus,* and *Rhizosolenia*, have all been well documented in previous studies (Rivkin et al.

1984; Villareal et al. 1999; Pilskaln et al. 2005). For a negative $PreNO_3$ anomaly to occur photosynthesis needs to occur in a layer where nitrate is not being consumed, since negative $PreNO_3$ anomalies occur when there is oxygen consumption without stoichiometric nitrate production. The whole migratory cycle of taxa of VMP has been estimated to take 4-5 days (Villareal et al. 1996).

Negative $PreNO_3$ anomalies were first observed in the North Pacific in 1995 by Emerson & Hayward 1995 where it was suggested that the remineralization of nitrogen poor DOM could potentially explain the occurrence of these anomalies. This suggestion was later supported by the findings of Abel et al. (2005), where their calculations for the magnitude of DOM remineralization and its non-Redfield and N-poor stoichiometry from observations in the subtropical North Pacific removed any anomalies for their calculations of $PreNO_3$. Then in 2010, Johnson et al., using the first Bio-Argo profiling floats equipped with both nitrate and oxygen sensors deployed near Station ALOHA in the subtropical North Pacific (HOT time series) observed the seasonal occurrence of negative preformed nitrate anomalies below the 1% light level. These authors attempted to link the summertime drawdown of dissolved inorganic carbon (DIC) in the surface mixed layer without the presence of sufficient amounts of nitrate and related it to negative $PreNO_3$ anomalies (Johnson et al. 2010). In Johnson et al. (2010), it was suggested that $PreNO_3$ anomalies could be caused by a dual physical and biological mechanism whereby synoptic vertical transport events at the base of the euphotic zone inject nitrate into the lower euphotic zone followed by VMP consuming this nitrate and then bringing it towards the surface to photosynthesize. VMP was suggested because the missing nitrate could not be moved by a fully physical mechanism because physical transport would also bring DIC to the surface, erasing the observed summertime DIC drawdown (Johnson et al. 2010).

In 2018, Letscher and Villareal formulated a new calculation of $PreNO_3$, termed residual $PreNO_3$, that accounts for non-Redfield stoichiometry as well as fractions of oxygen use attributed to the remineralization of DOM or sinking particulate organic matter (POM) (Eq. 1). The use of the residual $PreNO_3$ calculation aids in the identification of positive and negative $PreNO_3$ anomalies by accounting for the non-Redfield remineralization of DOM or POM that is known to exist in the subtropical ocean (Eq. 1; Letscher & Villareal, 2018). Thus the occurrence of residual $PreNO_3$ anomalies identify the presence of the two remaining non-Redfield biogeochemical processes: TEP cycling and VMP. As a result of TEP only accounting for a few percent of positive and negative $PreNO_3$ anomalies at the HOT and BATS time series sites, Letscher and Villareal suggested that VMP is most likely responsible for $PreNO_3$ anomaly formation. The results of Fawcett et al. (2018) working at the BATS site including isotopic evidence of nitrate consumption directly below the euphotic zone led them to suggest that vertical transport of TEP and subsequent TEP and nitrate consumption by bacteria below the euphotic zone is the most likely mechanism to be responsible for $PreNO_3$ anomalies. The analyses of Letscher & Villareal (2018) and Fawcett et al. (2018) have led them to opposing conclusions for the most likely mechanism responsible for $PreNO_3$ anomalies.

Two questions have been answered in the interest of investigating $PreNO_3$ anomalies as well as the mechanisms that lead to their formation:

1.) What is the seasonality and geographic extents of subsurface negative $PreNO_3$ anomalies and euphotic zone positive $PreNO_3$ anomalies in the global subtropical ocean?

2.) What biogeochemical processes capable of generating $PreNO_3$ anomalies are consistent with the seasonality and spatial extents found in the Bio-Argo float records?

Answers to both of these questions have been obtained by looking at spatiotemporal patterns in the occurrence of $PreNO_3$ anomalies as well as the rates in which $PreNO_3$ anomalies form. For the spatial extent of $PreNO_3$ anomalies, I hypothesized that they would be observed throughout the subtropical ocean. For the seasonally of $PreNO_3$ anomalies, I hypothesized that $PreNO_3$ anomalies would be stronger during the summer, based on observations form Letscher and Villareal 2018. For the mechanism that is responsible for $PreNO_3$ anomalies, I hypothesized that VMP consuming this nitrate at depth and then bringing it towards the surface to photosynthesize would be the more important mechanism for $PreNO_3$ anomaly formation.

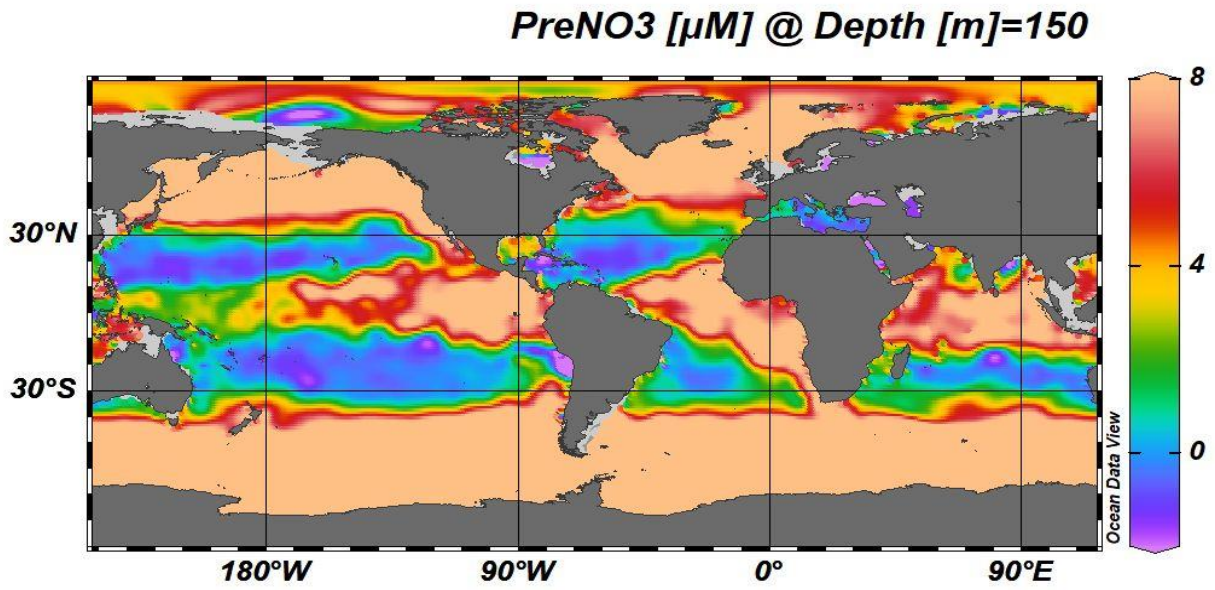

Figure 2. Annual average of $PreNO_3$ at 150m. $PreNO_3$ calculated using averages between ocean basin and depth specific constants (Table. 1; Letscher & Villareal, 2018). Data from World Ocean Atlas 2018 (Garcia et al. 2018).

Once Bio-Argo floats are deployed they start a ten-day cycle starting with an initial decent to 1000m where they take observations for roughly nine and a half days (Claustre et al. 2019). The Bio-Argo float then descends even further to 2000m before ascending to the surface to transmit its observations (Claustre et al. 2019). Originally data from 36 Bio-Argo floats were retrieved, however only 20 of the Bio-Argo floats were chosen mainly due to these floats

primarily taking observations between 40˚S and 40˚N. The reason that this latitudinal range was chosen is that negative PreNO3 anomalies primarily occur between 30˚S and 30˚N (Fig. 2).

CHAPTER I

METHODS

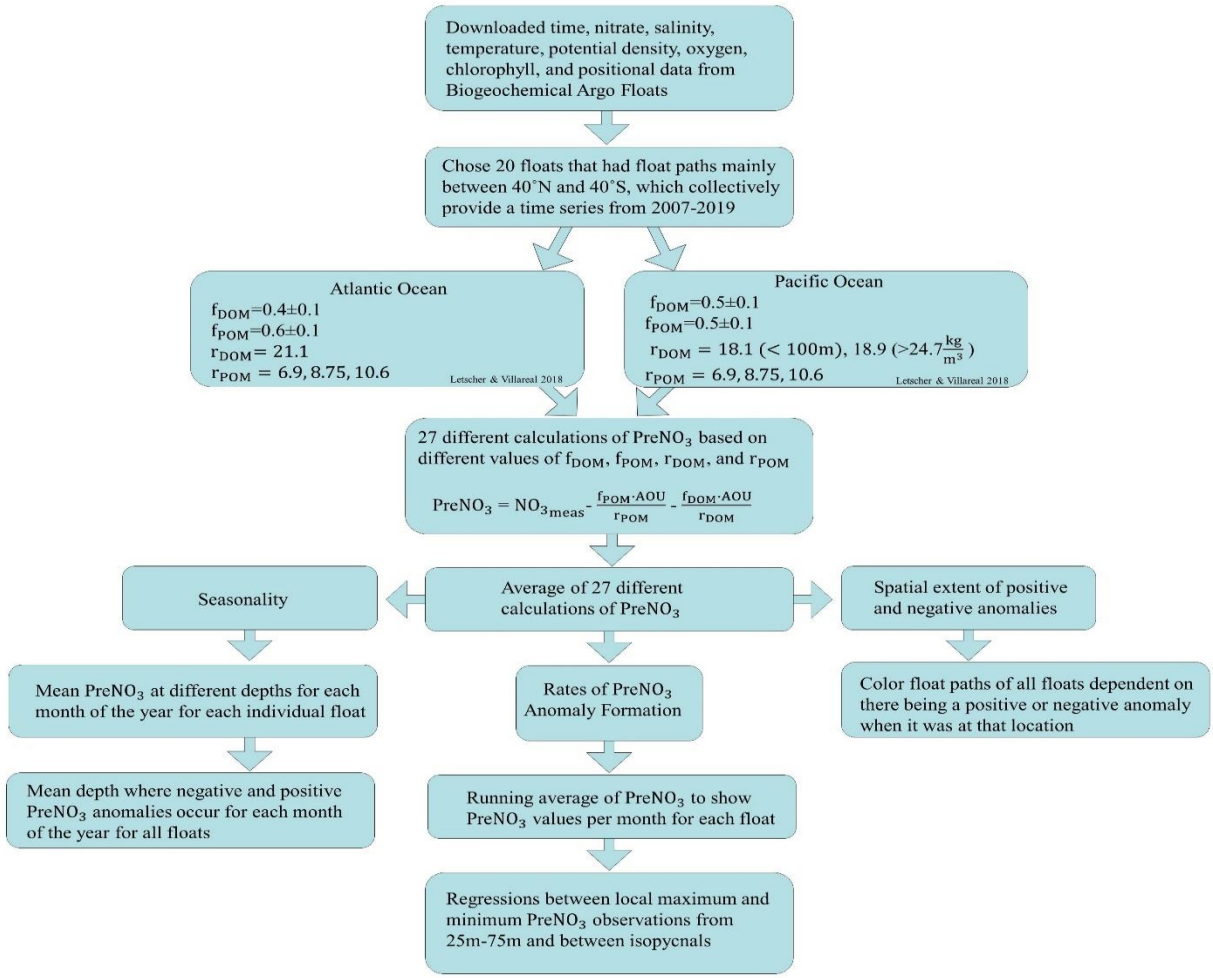

Figure 3. Flow chart of methods.

PreNO$_3$ Calculation

Twenty Biogeochemical Argo profiling floats were selected that traversed between 40ºN–40ºS for retrieval of observed nitrate, salinity, potential density, temperature, oxygen, time, and position. All observations from these Bio-Argo floats have associated quality flags for: good, questionable, bad, or missing or not inspected (MBARI 2017). The data quality flag for the

adjusted Bio-Argo data that was downloaded was 'Good Only' (MBARI 2017). Values of $PreNO_3$ were calculated using the formula residual $PreNO_3$ described in Letscher & Villareal, 2018 including ocean basin and depth specific constants (Table. 1):

$$\text{(Eq. 1) } PreNO_3 = NO_{3\,meas} - \frac{f_{POM} \cdot AOU}{r_{POM}} - \frac{f_{DOM} \cdot AOU}{r_{DOM}}$$

f_{POM} and f_{DOM} is the fraction of oxygen use attributable to POM and DOM remineralization, respectively (Eq. 1; Letscher & Villareal, 2018). r_{POM} and r_{DOM} is the ratio of oxygen used per mole of nitrogen for POM and DOM remineralization, respectively (Eq. 1; Letscher & Villareal, 2018). Apparent Oxygen Utilization (AOU) quantifies the oxygen saturation anomaly due to biological consumption or production of oxygen through respiration or photosynthesis, respectively, and was calculated using code written by Peltzer, 2007 (Eq. 1; Letscher & Villareal, 2018).

Table 1. Constants for the calculation of $PreNO_3$ and how they were varied for different depths, isopycnals, and oceans. Values based on Letscher & Villareal, 2018.

	Pacific				Atlantic			
	f_{DOM}	f_{POM}	r_{POM}	r_{DOM}	f_{DOM}	f_{POM}	r_{POM}	r_{DOM}
0-100m or $24.2\frac{kg}{m^3}$:$24.7\frac{kg}{m^3}$	0.5±0.1	0.5±0.1	10.6, 8.75, or 6.9	18.1	0.4±0.1	0.6±0.1	10.6, 8.75, or 6.9	21.1
σ_θ>$24.7\frac{kg}{m^3}$	0.5±0.1	0.5±0.1	10.6, 8.75, or 6.9	18.9	0.4±0.1	0.6±0.1	10.6, 8.75, or 6.9	21.1

$PreNO_3$ values were calculated using 27 different combinations of f_{DOM}, f_{POM}, r_{POM}, and r_{DOM} to capture the estimated uncertainty in each parameter, which is dependent on differences in depth, potential density, or ocean basin (Eq. 1; Table. 1; Fig. S1, S2; Letscher & Villareal, 2018). Note f_{DOM}, f_{POM}, and r_{DOM} were estimated empirically from time-series data at the HOT site in the subtropical North Pacific and the BATS site in the subtropical North Atlantic (Table. 1; Letscher & Villareal, 2018). The values of r_{POM} represent the minimum and maximum estimates from the published literature (Table. 1; Paulmier et al. 2009). Due to the differences in

the values used to calculate $PreNO_3$ in the Pacific and the Atlantic, there is more variability between the 27 different calculations of $PreNO_3$ in the Atlantic then there is in the Pacific (Table. 1; Fig. S1, S2) The 27 different calculations of $PreNO_3$ were averaged together to account for the variability that exists between the different calculations of $PreNO_3$ (Fig. S1, S2).

Rates of $PreNO_3$ Anomaly Formation

To calculate the rates of $PreNO_3$ anomaly formation, the average of the 27 different calculations of $PreNO_3$ was smoothed by a running average with a non-stationary window size dependent on the number of observations that were taken each individual month. 95% confidence intervals were calculated based on the standard error associated with averaging the 27 different values for $PreNO_3$ as well as the standard error for smoothing the time series. Regressions were then calculated between local maxima and minima of $PreNO_3$ observations using method of least squares. Local minima and maxima were identified for each year by using the Matlab™ function, *islocalmax*, with the absolute smoothed $PreNO_3$ values as the input (The MathWorks™, Inc.). The input argument *MinSeparation* was used to specify the minimum distance between points that were identified as local maxima or minima (The MathWorks™, Inc.). The argument *MaxNumExtrema* was used to set the maximum number of minima or maxima that would be identified for each year (The MathWorks™, Inc.). The number of regressions for each time series as well as the length of the regressions were specified by using the combination of these input arguments. To avoid the introduction of any bias the values for *MaxNumExtrema* and *MinSeparation* were kept the same for all profiling floats to determine the rates of $PreNO_3$ anomaly formation. The net $PreNO_3$ magnitude was calculated by taking the sum of the products of the length of the regressions in days by the rates of $PreNO_3$ anomaly formation (Table. 2). Mean rates of positive and negative $PreNO_3$ anomaly formation were determined by

taking averages of positive and negative rates of $PreNO_3$ anomaly formation for each Bio-Argo regional group based on float name within 25m to 75m, the middle layers, and bottom layers from Table. 2 (Table. 3).

Spatial Extent & Seasonality of $PreNO_3$ Anomalies

The seasonality of $PreNO_3$ anomalies was determined for the Bio-Argo floats that remained in the northern hemisphere in terms of: the $PreNO_3$ values, spatial extent of $PreNO_3$ anomalies, and the depths at which positive and negative $PreNO_3$ anomalies occurred. The spatial extent of $PreNO_3$ anomalies was determined by using the *Mapping Toolbox* from Matlab™ (The MathWorks™, Inc.). The occurrence of positive and negative $PreNO_3$ anomalies geographically as well as with depth were ascertained by plotting locations where $PreNO_3$ estimates were available for each individual Bio-Argo float (Fig. 10, 11). The points for each location were then differentiated by color dependent if a positive or negative $PreNO_3$ anomaly occurred at the locations where $PreNO_3$ was able to be derived (Fig. 10, 11). The seasonality of $PreNO_3$ values was determined by grouping all the northern hemisphere floats by their float names and then taking monthly averages of each group's $PreNO_3$ values between 25m to 75m as well as between isopycnals that outlined where negative $PreNO_3$ anomalies occurred (Fig. 8). The seasonality of the depths where a negative $PreNO_3$ anomaly occurred were determined by taking monthly averages of depths in the first 350m of the water column where the core of the negative $PreNO_3$ anomalies occurred (Fig. 12). The seasonality of the depths where a positive $PreNO_3$ anomaly occurred were determined by taking monthly averages of depths above where negative $PreNO_3$ anomalies occurred (Fig. 12).

Interannual Variability

The interannual variability of $PreNO_3$ and ocean temperature were determined by using a combined and chronologically sorted time series that included the data sets of all North Pacific Bio-Argo floats. Using this time series, the interannual variability of the thickness of the layer where negative $PreNO_3$ anomalies occurred was determined. This was accomplished by taking the difference between the deepest and shallowest depths where negative $PreNO_3$ anomalies occurred for each year from 2007 to 2017 (Fig. S36). For comparison, yearly averages for the values for $PreNO_3$ and ocean temperatures were performed as well (Fig. S36).

CHAPTER II

RESULTS

$PreNO_3$

North Pacific

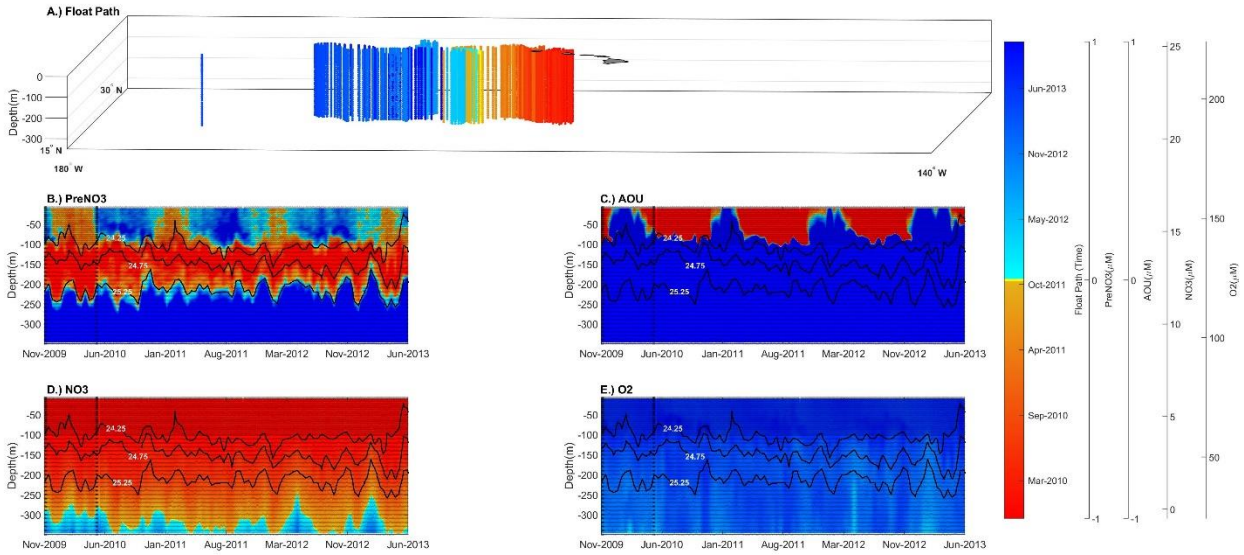

Figure 4. A.) Float path of Hawaii 6401 colored by time. B.) $PreNO_3$ for the first 350m of water column along float path from Nov-09 to Nov-13, C.) AOU for the first 350m of water column along float path. D.) NO_3 for the first 350m of water column along float path. E.) O_2 for the first 350m of water column along float path. Black lines in B:E represent isopycnals, 24.25$\frac{kg}{m^3}$, 24.75$\frac{kg}{m^3}$, and 25.25$\frac{kg}{m^3}$, chosen to outline anomalies. Dots in B:E represent observations. $PreNO_3$ and AOU limited to -1:1.

South Pacific

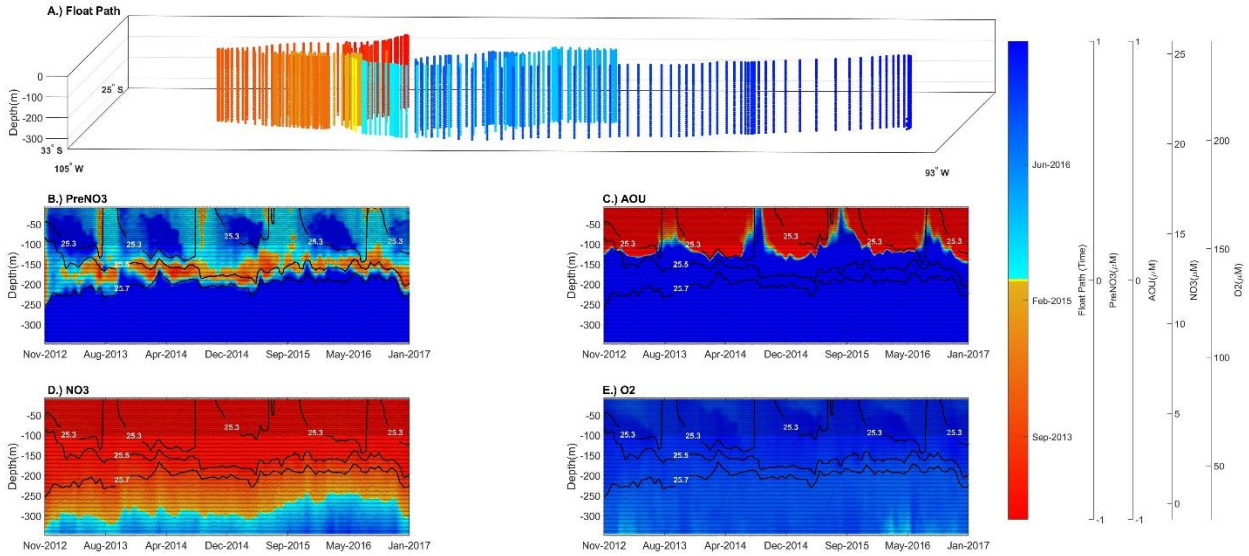

Figure 5. A.) Float path of SOPACIFIC 7553 colored by time. B.) PreNO$_3$ for the first 350m of water column along float path from Nov-12 to Sep-17, C.) AOU for the first 350m of water column along float path. D.) NO$_3$ for the first 350m of water column along float path. E.) O$_2$ for the first 350m of water column along float path. Black lines in B:E represent isopycnals 25.3$\frac{kg}{m^3}$, 25.5$\frac{kg}{m^3}$, and 25.7$\frac{kg}{m^3}$, chosen to outline anomalies. Dots in B:E represent observations. PreNO$_3$ and AOU limited to -1:1.

North Atlantic

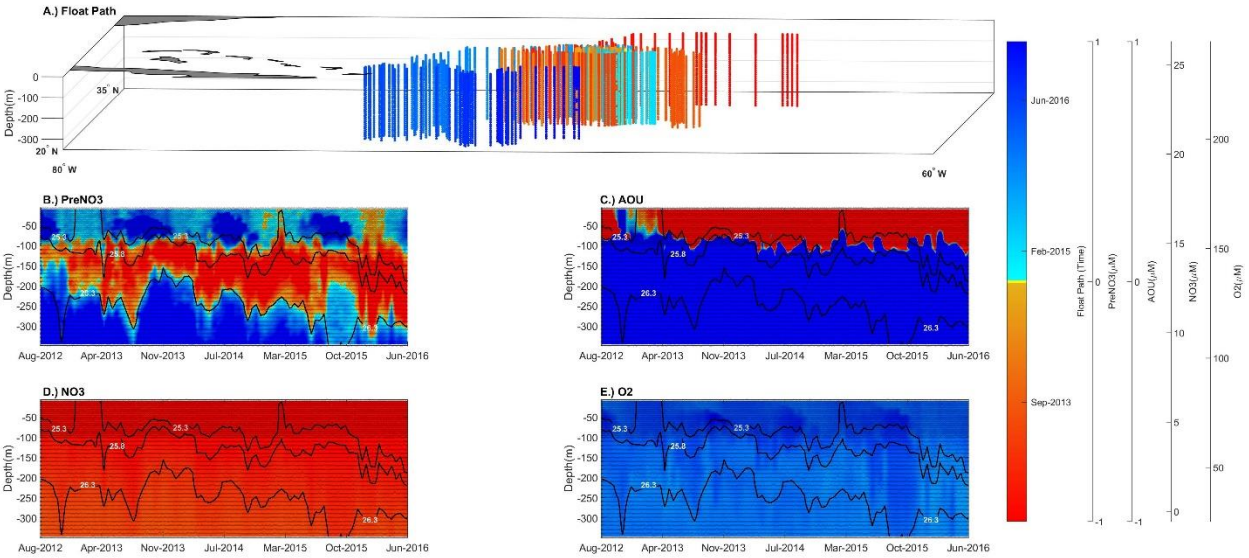

Figure 6. A.) Float path of Bermuda 7663 colored by time. B.) PreNO$_3$ for the first 350m of water column along float path from Aug-12 to Dec-16, C.) AOU for the first 350m of water column along float path. D.) NO$_3$ for the first 350m of water column along float path. E.) O$_2$ for the first 350m of water column along float path. Black lines in B:E represent isopycnals 25.3$\frac{kg}{m^3}$, 25.8$\frac{kg}{m^3}$, and 26.3$\frac{kg}{m^3}$, chosen to outline anomalies. Dots in B:E represent observations. PreNO$_3$ and AOU limited to -1:1.

In the upper 100m (i.e. the approximate euphotic zone) of most float records there is a general trend of swapping between negative $PreNO_3$ anomalies present in the Winter and positive $PreNO_3$ anomalies for the rest of the year (Fig. 4, 5, 6). AOU showed net photosynthesis (negative values) in the upper 100m, with episodes of transitioning to net respiration (positive values) during the Winter due to convective mixing (Fig. 4, 5, 6). Observations of NO_3 and O_2 from all floats followed expected trends where NO_3 increases with depth and O_2 decreases with depth (Fig. 4, 5, 6). All profiling floats had positive $PreNO_3$ anomalies ($PreNO_3>0$) in the upper ocean (<~100m) and typically exhibited negative $PreNO_3$ anomalies ($PreNO_3<0$) at depths of ~100m-250m, however negative $PreNO_3$ anomalies were not as prevalent in the records from the EQPACW 12788 and CALCURRENT 7647 compared to the other profiling floats (Fig. S20, S24). Whereas EQPACW 8474 and CALCURRENT 7618 did have negative $PreNO_3$ anomalies in their records (Fig. S18, S22). The CALCURRENT float observations did not match up in terms of time, but the EQPACW floats did have one instance where they did (Fig. S18, S20, S22, S24). However at the time of this observation the two EQPACW floats were in two totally different locations (Fig. S22, S24).

Rates of $PreNO_3$ Anomaly Formation

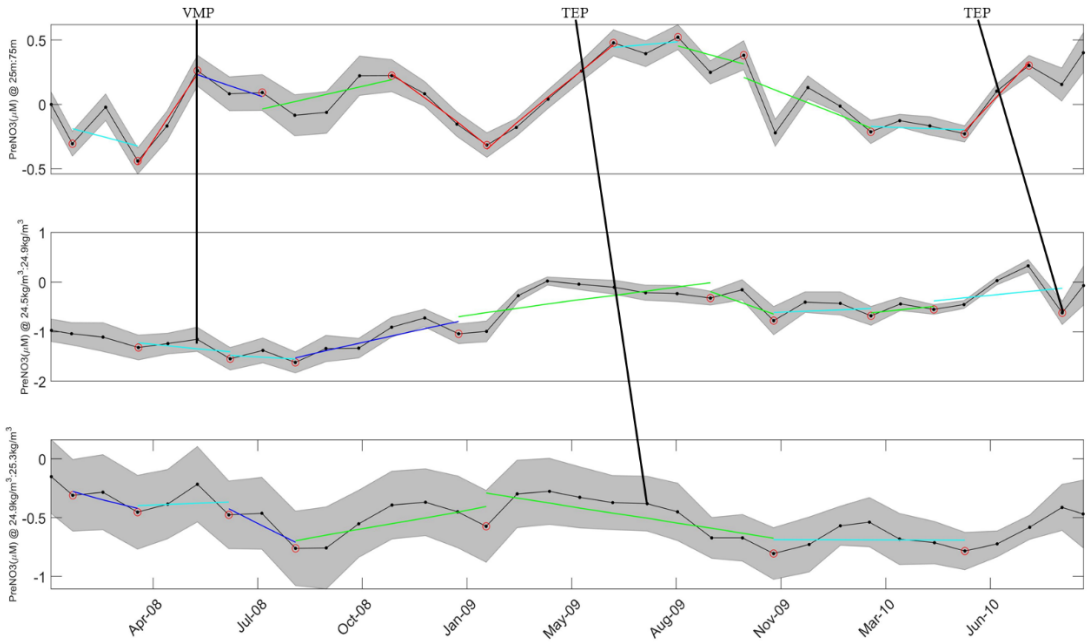

Figure 7. $PreNO_3$ for Hawaii 5145 smoothed to show $PreNO_3$ per month with regression of $PreNO_3$ vs time. Top figure $PreNO_3$ at 25m-75m, middle figure $PreNO_3$ at $24.5\frac{kg}{m^3}$:$24.9\frac{kg}{m^3}$, and bottom figure $PreNO_3$ at $24.9\frac{kg}{m^3}$:$25.3\frac{kg}{m^3}$. Black dots are observations and the ones with red circles are local minima and maxima. Regressions colored by the value of the correlation coefficient; r^2>0.75(Red), 0.75> r^2>0.5(Blue), 0.5> r^2>0.25(Green), 0.25> r^2>0(Cyan). Grey regions represent 95% confidence intervals for $PreNO_3$ values. Black lines on figures indicate observations where TEP or VMP may have been responsible.

Table 2. For observations between 25:75m and the chosen isopycnals the mean; Location, Rates of Positive and Negative $PreNO_3$ anomaly formation, Length of regressions in days and r^2 for regressions of $PreNO_3$ concentration versus time, for each individual float. NA indicates that no positive or negative rates of anomaly formation were observed.

Float Name	Layer	Mean Location	Mean Positive $PreNO_3$ Rate ($\frac{\mu mol\ N}{m^3\ day}$)	Mean Negative $PreNO_3$ Rate ($\frac{\mu mol\ N}{m^3\ day}$)	Mean Length of Positive Trends (days)	Mean Length of Negative Trends (days)	Net $PreNO_3$ Magnitude ($\frac{mmol\ N}{m^3}$)	Mean r^2
Hawaii 5145	25m to 75m	22.87 °N,157.99°W	5.91±2.04	-2.82±0.77	84.80±15.21	81.67±9.64	0.84	0.54±0.12
	$24.5\frac{kg}{m^3}$:$24.9\frac{kg}{m^3}$	22.87 °N,157.99°W	2.55±0.65	-3.53±1.97	134.40±31.01	70.00±8.50	1.20	0.28±0.08
	$24.9\frac{kg}{m^3}$:$25.3\frac{kg}{m^3}$	22.87 °N,157.99°W	0.96±0.63	-2.12±0.98	134.50±47.50	145.75±51.26	-0.51	0.38±0.12
Hawaii 6401	25m to 75m	22.69 °N,157.99°W	4.30±1.01	-5.68±1.64	147.83±21.57	106.00±15.04	1.45	0.76±0.09
	$24.25\frac{kg}{m^3}$:$24.75\frac{kg}{m^3}$	22.69 °N,157.99°W	2.19±0.58	-3.76±1.00	125.43±16.55	103.80±13.14	0.15	0.26±0.07
	$24.75\frac{kg}{m^3}$:$25.25\frac{kg}{m^3}$	22.69 °N,157.99°W	1.34±0.60	-1.33±0.41	144.75±19.90	80.67±9.35	1.12	0.28±0.08
Hawaii 6891	25m to 75m	22.68 °N,157.99°W	1.68±0.76	-3.65±2.13	142.67±25.64	61.33±1.33	0.08	0.29±0.11
	$24.1\frac{kg}{m^3}$:$24.6\frac{kg}{m^3}$	22.68 °N,157.99°W	3.21±2.41	-0.70±0.26	121.33±29.38	83.00±22.01	0.82	0.25±0.16
	$24.6\frac{kg}{m^3}$:$25.1\frac{kg}{m^3}$	22.68 °N,157.99°W	4.33±0.96	-7.26±0.75	115.25±18.73	74.50±16.50	0.94	0.62±0.06
Hawaii 8497	25m to 75m	22.82°N,157.89°W	2.17±0.88	-2.76±0.92	151.00±53.13	140.80±24.78	-0.85	0.62±0.12
	$24.2\frac{kg}{m^3}$:$24.75\frac{kg}{m^3}$	22.82°N,157.89°W	3.32±0.54	-2.53±0.80	94.00±17.62	111.22±12.59	-1.52	0.31±0.09
	$24.75\frac{kg}{m^3}$:$25.3\frac{kg}{m^3}$	22.82°N,157.89°W	2.50±0.85	-1.23±0.39	81.86±9.17	118.00±8.94	0.51	0.55±0.10
Hawaii 8486	25m to 75m	22.68°N,158.04°W	4.88±1.43	-5.26±2.07	84.80±11.08	101.33±27.55	0.27	0.67±0.15
	$24.5\frac{kg}{m^3}$:$24.8\frac{kg}{m^3}$	22.68°N,158.04°W	2.64±0.98	-1.74±1.02	113.50±24.75	92.67±17.61	0.88	0.31±0.12
	$24.8\frac{kg}{m^3}$:$25\frac{kg}{m^3}$	22.68°N,158.04°W	1.46±0.94	-2.17±0.42	135.00±47.42	94.50±29.50	0.38	0.21±0.08
Hawaii 6403	25m to 75m	22.70°N,158.12°W	4.60±1.19	-5.61±0.90	187.40±53.50	140.50±5.50	2.24	0.70±0.12
	$24.3\frac{kg}{m^3}$:$24.8\frac{kg}{m^3}$	22.70°N,158.12°W	4.94±1.18	-3.00±1.31	97.57±13.46	180.00±44.57	1.82	0.51±0.09
	$24.8\frac{kg}{m^3}$:$25.2\frac{kg}{m^3}$	22.71°N,158.12°W	2.72	-0.78±0.31	154.00	173.71±21.70	-0.44	0.30±0.13
Bermuda 6391	25m to 75m	31.74°N,64.32°W	6.69±0.50	-4.29±1.88	122.00±29.00	136.75±29.14	-0.20	0.76±0.11
	$25.5\frac{kg}{m^3}$:$25.9\frac{kg}{m^3}$	31.74°N,64.32°W	8.41±3.60	-8.21±4.93	195.67±15.86	76.50±6.96	2.49	0.67±0.10
	$25.9\frac{kg}{m^3}$:$26.3\frac{kg}{m^3}$	31.74°N,64.32°W	5.60±1.41	-10.49±4.21	198.67±46.35	96.00±24.42	0.04	0.80±0.09
Bermuda 6976	25m to 75m	31.76°N,64.16°W	12.15±3.45	-6.69±1.74	199.00±69.95	100.13±15.47	-0.32	0.54±0.08
	$25.4\frac{kg}{m^3}$:$25.9\frac{kg}{m^3}$	31.76°N,64.16°W	10.69±2.58	-18.09±5.81	199.00±84.79	151.00±2.00	5.68	0.63±0.12
	$25.9\frac{kg}{m^3}$:$26.3\frac{kg}{m^3}$	31.76°N,64.16°W	20.64±11.44	-13.39±1.82	176.00±63.06	145.00±38.46	-4.67	0.62±0.08
Bermuda 6975	25m to 75m	31.61°N,64.22°W	15.61±3.77	-5.71±1.65	117.14±20.15	102.33±26.03	8.98	0.51±0.10
	$25.2\frac{kg}{m^3}$:$25.8\frac{kg}{m^3}$	31.61°N,64.22°W	18.63±14.98	-8.06±4.11	107.25±37.70	144.00±44.67	-1.23	0.38±0.12
	$25.8\frac{kg}{m^3}$:$26.3\frac{kg}{m^3}$	31.61°N,64.22°W	16.36±8.49	-5.92±1.07	99.00±20.55	128.60±30.34	1.57	0.52±0.10
Bermuda 7663	25m to 75m	31.73°N,64.20°W	5.74±1.10	-7.06±2.62	164.60±28.47	109.00±20.96	0.24	0.72±0.09
	$25.3\frac{kg}{m^3}$:$25.8\frac{kg}{m^3}$	31.73°N,64.20°W	12.25±4.16	-12.37±3.99	102.60±16.29	92.00±15.14	-2.88	0.65±0.08
	$25.8\frac{kg}{m^3}$:$26.3\frac{kg}{m^3}$	31.73°N,64.20°W	2.13±0.99	-4.20±1.27	83.00±20.50	147.75±26.58	-3.33	0.31±0.07
ETNP 6960	25m to 75m	14.88°N,123.23°W	3.57±0.72	-3.49±1.37	122.33±7.64	96.60±22.37	1.21	0.45±0.10
	$24\frac{kg}{m^3}$:$25.3\frac{kg}{m^3}$	14.88°N,123.23°W	4.09±1.03	-5.17±1.96	82.50±7.96	99.60±5.64	-0.12	0.27±0.08
	$25.3\frac{kg}{m^3}$:$26.6\frac{kg}{m^3}$	14.88°N,123.23°W	11.92±7.48	-9.32±2.89	100.75±7.42	116.71±15.19	-2.29	0.38±0.11
ETNP 7558	25m to 75m	13.99°N,123.34°W	NA	-11.07	NA	183.00	-2.03	0.75
	$24\frac{kg}{m^3}$:$25.3\frac{kg}{m^3}$	13.99°N,123.34°W	6.15	-17.89	94.00	151.00	-2.12	0.69±0.19
	$25.3\frac{kg}{m^3}$:$26.6\frac{kg}{m^3}$	13.99°N,123.34°W	19.82	-25.49	145.00	152.00	-1.00	0.94±0.03
CALCURRENT 7618	25m to 75m	31.89°N,124.10°W	2.97±1.12	-3.83±1.48	107.71±21.80	102.17±15.39	-1.04	0.48±0.12
	$24.4\frac{kg}{m^3}$:$24.9\frac{kg}{m^3}$	31.89°N,124.10°W	3.87±1.26	-5.91±1.84	97.88±17.55	97.33±4.00	-0.77	0.61±0.08
	$24.9\frac{kg}{m^3}$:$25.3\frac{kg}{m^3}$	31.89°N,124.10°W	5.30±1.91	-6.45±2.28	79.50±6.02	153.33±19.36	-3.38	0.49±0.12
CALCURRENT 7647	25m to 75m	35.15°N,122.90°W	14.40±11.25	-17.85±11.44	141.33±9.67	175.50±38.04	-2.61	0.55±0.13
	$24.6\frac{kg}{m^3}$:$24.8\frac{kg}{m^3}$	35.15°N,122.90°W	10.92±5.42	-7.75±2.40	97.67±18.11	178.00±44.43	-3.35	0.59±0.10
	$24.8\frac{kg}{m^3}$:$25\frac{kg}{m^3}$	35.15°N,122.90°W	13.83±5.00	-34.15±18.15	116.75±19.26	150.50±35.09	-8.15	0.72±0.09
EQPACW 8474	25m to 75m	8.02°S,155.00°W	8.24±5.13	NA	121.50±1.50	NA	1.99	0.49±0.30
	$23.4\frac{kg}{m^3}$:$24\frac{kg}{m^3}$	8.02°S,155.00°W	17.62	NA	209.00	NA	3.68	0.77
	$24\frac{kg}{m^3}$:$24.6\frac{kg}{m^3}$	8.02°S,155.00°W	10.88±0.65	NA	137.50±14.50	NA	3.01	0.79±0.09
EQPACW 12788	25m to 75m	4.00°S,170.05°W	NA	-6.26	NA	213.00	-1.33	0.80
	$22.9\frac{kg}{m^3}$:$23.3\frac{kg}{m^3}$	4.00°S,170.05°W	NA	-2.43	NA	147.00	-0.36	0.06
	$23.3\frac{kg}{m^3}$:$23.7\frac{kg}{m^3}$	4.00°S,170.05°W	11.59	-29.91	54.00	71.00	-1.50	0.38±0.28
KUROSHIO 7546	25m to 75m	33.48°N,147.61°E	16.32±5.17	-13.77±8.15	129.50±29.64	128.20±22.26	1.98	0.68±0.07
	$24\frac{kg}{m^3}$:$24.5\frac{kg}{m^3}$	33.48°N,147.61°E	12.69±3.62	-10.64±4.33	171.00±25.26	205.00±99.00	5.52	0.70±0.10
	$24.5\frac{kg}{m^3}$:$25\frac{kg}{m^3}$	33.48°N,147.61°E	12.37±4.65	-6.33±2.21	87.57±14.52	96.40±15.29	6.32	0.59±0.10
KUROSHIO 7674	25m to 75m	36.98°N,148.69°E	8.67±3.18	-15.63±3.09	121.83±27.45	97.20±17.48	0.39	0.34±0.09
	$23.8\frac{kg}{m^3}$:$24.7\frac{kg}{m^3}$	36.98°N,148.69°E	13.38±6.05	-4.79±3.52	218.00±116.69	168.00±60.37	4.39	0.36±0.14
	$24.7\frac{kg}{m^3}$:$25.3\frac{kg}{m^3}$	36.98°N,148.69°E	9.38±3.73	-9.15±2.18	97.17±21.15	82.57±8.03	-0.70	0.32±0.07
NOPACIFIC 7642	25m to 75m	36.56°N,158.01°W	5.42	-0.44	243.00	121.00	1.27	0.23±0.20
	$25\frac{kg}{m^3}$:$25.3\frac{kg}{m^3}$	36.56°N,158.01°W	28.69	-5.46	303.00	59.00	8.37	0.68±0.04
	$25.3\frac{kg}{m^3}$:$25.6\frac{kg}{m^3}$	36.56°N,158.01°W	14.73±7.76	NA	180.50±86.50	NA	6.66	0.73±0.19
SOPACIFIC 7553	25m to 75m	28.01 °S,101.51°W	2.30±0.74	-4.13±1.19	137.60±31.97	215.00±44.73	-0.91	0.52±0.11
	$25.3\frac{kg}{m^3}$:$25.5\frac{kg}{m^3}$	28.01 °S,101.51°W	2.37±1.32	-2.88±0.60	126.83±26.12	102.38±12.88	-0.83	0.52±0.10
	$25.5\frac{kg}{m^3}$:$25.7\frac{kg}{m^3}$	28.01 °S,101.51°W	7.45±1.51	-4.23±1.22	94.11±11.41	106.63±17.20	1.35	0.58±0.07

KUROSHIO 7546 had the greatest mean positive rate of $PreNO_3$ anomaly formation within 25:75m at, 16.32±5.17 $\frac{\mu mol\ N}{m^3\ day}$ (Table. 2). NOPACIFIC 7642 had the greatest mean length of positive trends of $PreNO_3$ anomaly formation within 25:75m at, 243 days (Table. 2). Whereas Bermuda 6976 had the greatest mean positive rate of $PreNO_3$ anomaly formation between the deepest layers analyzed out of the profiling floats at, 20.64±11.44 $\frac{\mu mol\ N}{m^3\ day}$ (Table. 2). Bermuda 6391 had the greatest mean length of positive trends of $PreNO_3$ anomaly formation between the deepest layers at, 198.67±46.35 days (Table. 2).

CALCURRENT 7647 had the greatest mean negative rate of $PreNO_3$ anomaly formation within 25:75m at, -17.85±11.44 $\frac{\mu mol\ N}{m^3\ day}$ (Table. 2). SOPACIFIC 7642 had the greatest mean length of negative trends of $PreNO_3$ anomaly formation within 25:75m at, 215.00±44.73 days (Table. 2). Whereas CALCURRENT 7647 had the greatest mean negative rate of $PreNO_3$ anomaly formation between the deepest layers analyzed out of the profiling floats at, -34.15±18.15 $\frac{\mu mol\ N}{m^3\ day}$ (Table. 2). Hawaii 6403 had the greatest mean length of negative trends of $PreNO_3$ anomaly formation between the deepest layers at, 173.71±21.70 days (Table. 2). The Bermuda and CALCURRENT Bio-Argo floats both had 6 negative net $PreNO_3$ magnitude values, which was the most out of all the Bio-Argo float groups (Table. 2). It is worth noting that all the layers for both CALCURRENT Bio-Argo floats had negative net $PreNO_3$ magnitude values (Table. 2).

Spatial Extent & Seasonality of $PreNO_3$

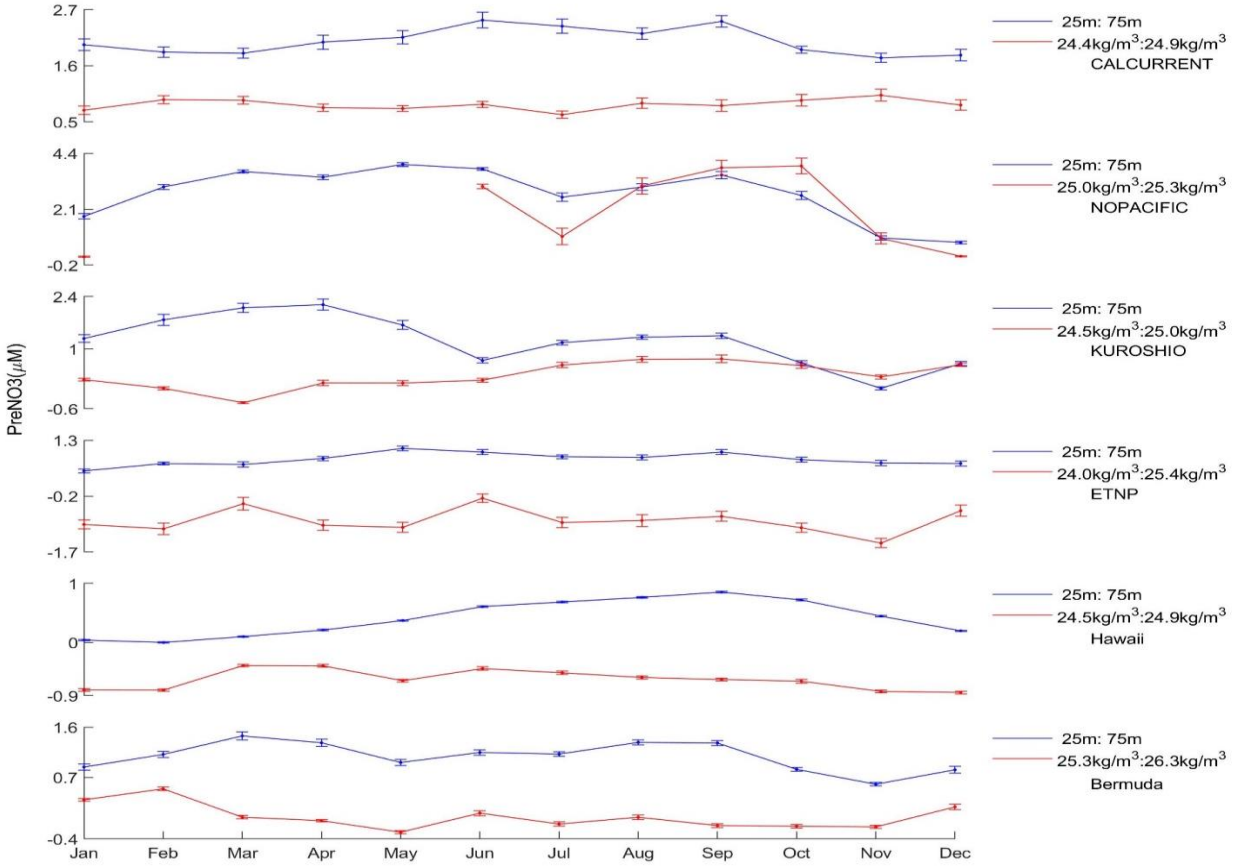

Figure 8. Seasonality of $PreNO_3$ observations from groups of Bio-Argo floats based on float name. Only floats that stayed in the Northern Hemisphere were included. Blue lines are observations 25m to 75m. Red lines are observations taken between chosen isopycnals.

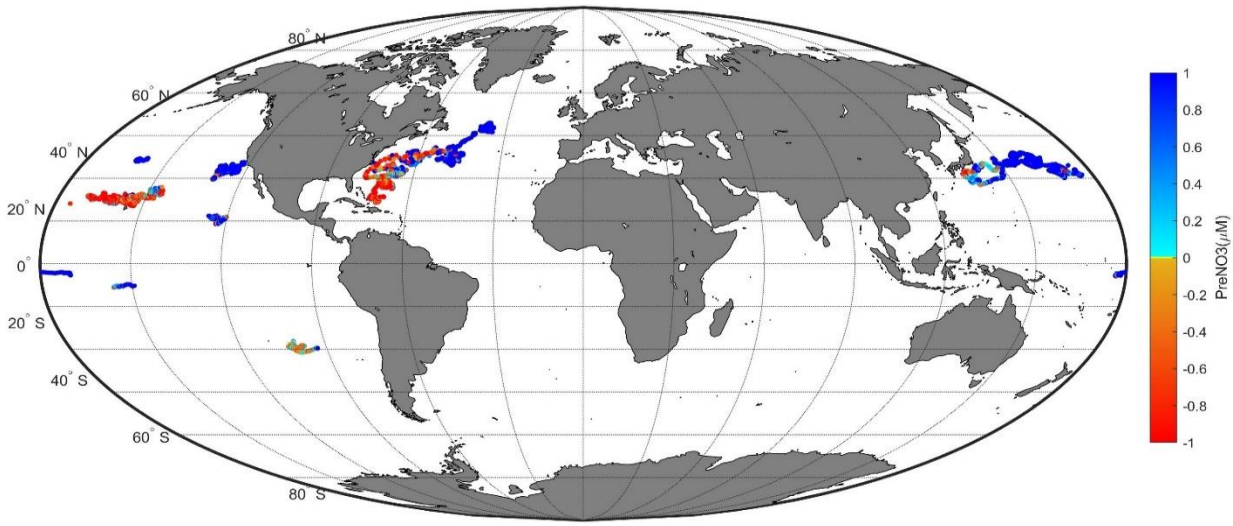

Figure 9. $PreNO_3$ anomalies from 100m:150m along float paths of the 20 Bio-Argo floats from 2007:22019. $PreNO_3$ limited to -1:1.

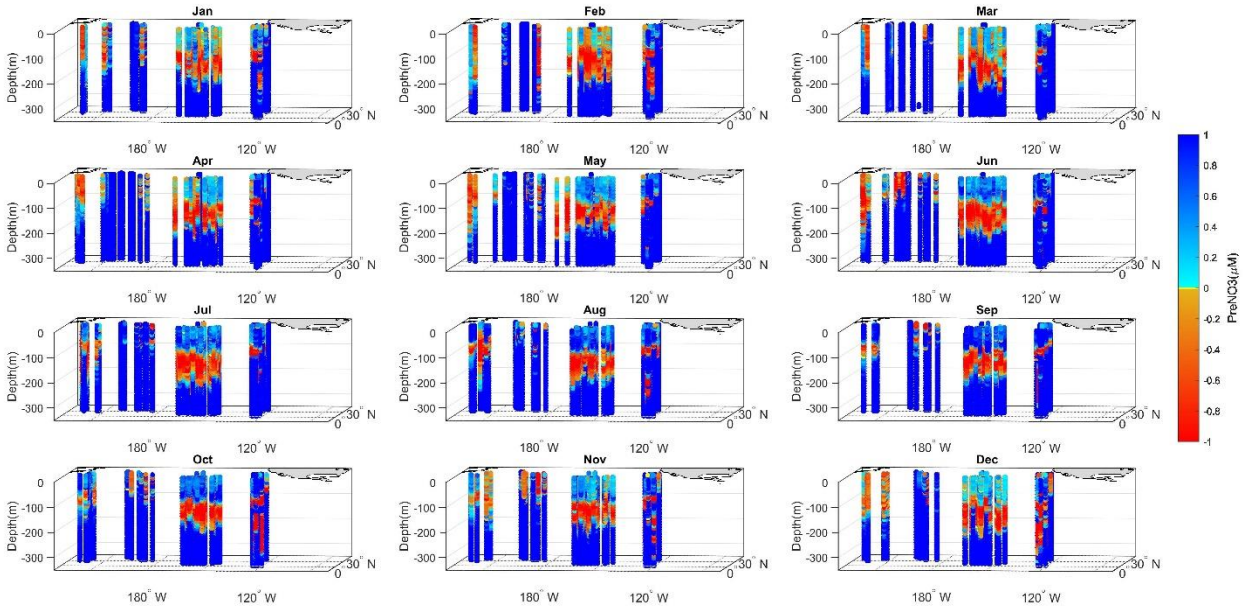

Figure 10. The seasonality of the occurrence of negative or positive $PreNO_3$ anomalies in the North Pacific in the first 350m of the water column. $PreNO_3$ limited to -1:1.

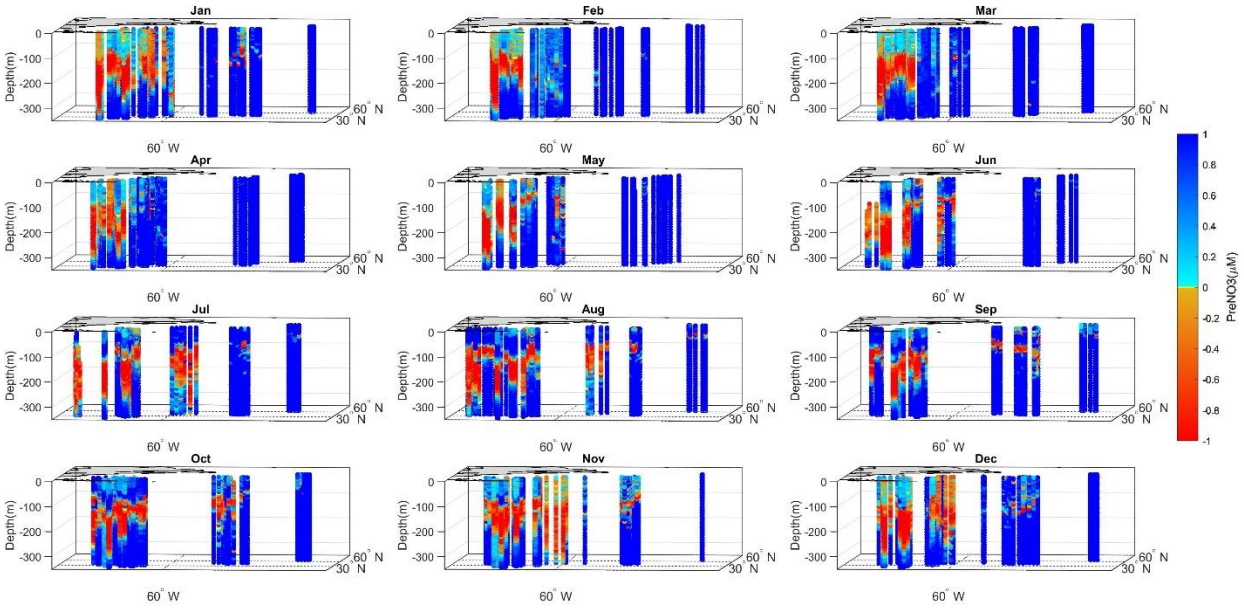

Figure 11. The seasonality of the occurrence of negative or positive $PreNO_3$ anomalies in the North Atlantic in the first 350m of the water column. $PreNO_3$ limited to -1:1.

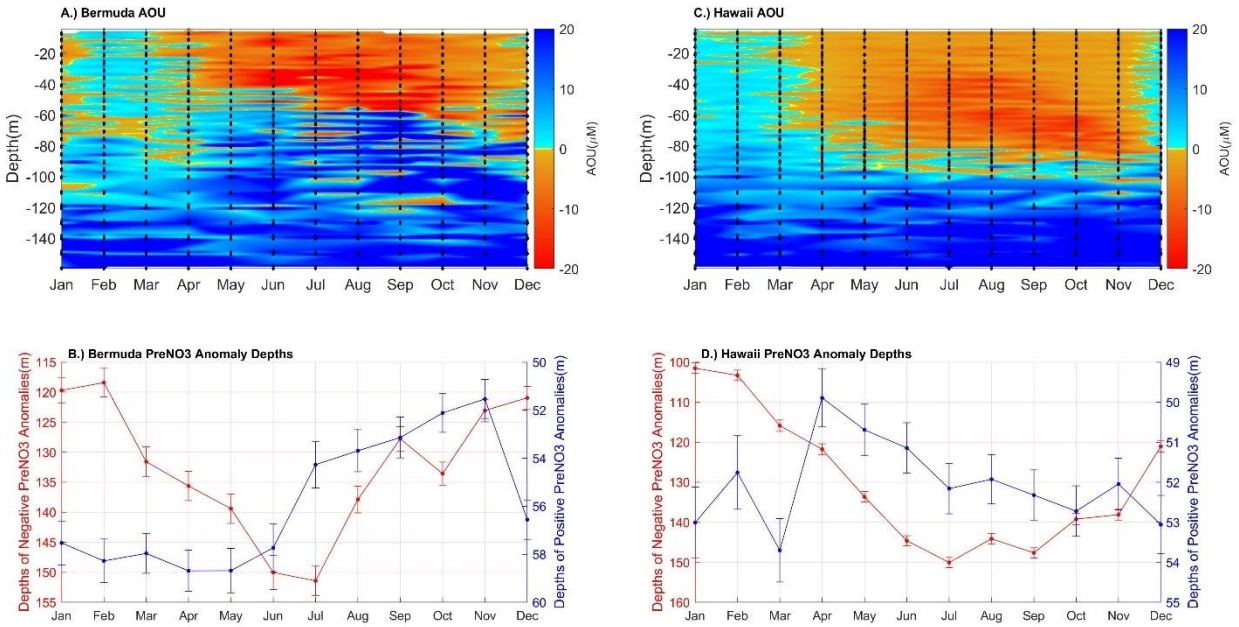

Figure 12. Bermuda and Hawaii seasonal AOU vs $PreNO_3$ anomaly depths. A.) Monthly AOU derived from Bermuda Bio-Argo float observations for 0m-160m. B.) Monthly depths of core of negative $PreNO_3$ anomalies within 0m:350m (red) and of positive $PreNO_3$ anomalies above negative $PreNO_3$ anomalies (blue) from Bermuda Bio-Argo floats. C.) Monthly AOU derived from Hawaii Bio-Argo float observations for 0m-160m. D.) Monthly depths of core of negative $PreNO_3$ anomalies within 0m:350m (red) and of positive $PreNO_3$ anomalies above negative $PreNO_3$ anomalies (blue) from Bermuda Bio-Argo floats. Black dots in A.) and C.) represent observations.

For the California Current $PreNO_3$ values increase in the Winter and Spring whereas they decrease in the Summer and Fall at 25m:75m (Fig. 8). Where at depth $PreNO_3$ values increase during the Winter, Summer, and Fall whereas they decrease during the Spring (Fig. 8). North of Hawaii (NOPACIFIC) $PreNO_3$ values increase in the Winter and Spring whereas they decrease in the Summer and Fall at 25m:75m (Fig. 8). Where at depth $PreNO_3$ values increase during the Summer whereas they decrease during the Fall (Fig. 8). For the Kuroshio Current $PreNO_3$ values increase in the Winter and Summer whereas they decrease in the Fall and Spring at 25m:75m (Fig. 8). Where at depth $PreNO_3$ values increase during the Spring and Summer whereas they decrease during the Fall and Winter (Fig. 8). For the East Tropical North Pacific (ETNP) $PreNO_3$ values increase in the Spring whereas they decrease in the Winter, Summer and Fall at 25m:75m (Fig. 8). Where at depth $PreNO_3$ values increase during every season (Fig. 8). For Hawaii $PreNO_3$ values increase in the Spring and Summer whereas they decrease in the Winter and

Fall at 25m:75m (Fig. 8). Where at depth $PreNO_3$ values increase during the Winter whereas they decrease during the Spring, Summer and Fall (Fig. 8). For Bermuda $PreNO_3$ values increase in the Winter and Summer whereas they decrease in the Fall and Spring at 25m:75m (Fig. 8). Where at depth $PreNO_3$ values shows the same seasonal trend that is seen at 25m:75m (Fig. 8). There being no values for the NOPACIFIC float during the Winter and Spring months is likely due to the isopycnal contours shoaling to the surface (Fig. 8, S34). NOPACIFIC had the most positive $PreNO_3$ values whereas ETNP had the most negative $PreNO_3$ values (Fig. 8).

$PreNO_3$ values derived within 100m:150m from the Bio-Argo floats indicate that negative $PreNO_3$ anomalies did not occur outside of the latitudinal range between 40˚S and 40˚N (Fig. 9). Generally in the North Pacific, the negative $PreNO_3$ anomalous layer retreats below 100m starting in July and then starts shoaling towards the surface again starting in November (Fig. 10). In the North Atlantic, the negative $PreNO_3$ anomalous layer retreats below 100m starting in June and then start moving towards the surface again starting in November (Fig. 11). Positive $PreNO_3$ anomalies appear around Bermuda beginning at about 58m in January and shoal to approximately 54m by July, followed by an increase in depth to roughly 57m by December (Fig. 12). Whereas negative $PreNO_3$ anomalies appear around Bermuda beginning at about 120m in January and increase to roughly 150m depth by June, followed by shoaling back to approximately 120m by December (Fig. 12). Positive $PreNO_3$ anomalies appear around Hawaii beginning at about 53m in January and shoal to approximately 51m by May, followed by an increase in depth back to roughly 53m by December (Fig. 12). Whereas negative $PreNO_3$ anomalies appear around Hawaii beginning at about 102m in January and increase to roughly 150m depth by July, followed by shoaling back to approximately 120m by December (Fig. 12). Changes in the monthly averaged depths of the core of positive and negative $PreNO_3$ anomalies

are tracked relatively well by changes in AOU around Bermuda (Fig. 12). However the monthly averaged depths of the core of positive $PreNO_3$ anomalies does not coincide with changes in AOU around Hawaii (Fig. 12).

Interannual Variability

In 2007 the thickness of the layer where negative $PreNO_3$ anomalies occurred in the North Pacific was roughly 245m (Fig. S36). For the same year the average value for $PreNO_3$ inside of the negative anomaly layer was about -0.72µM and the average ocean temperature was approximately 20.43˚C (Fig. S36). The thickness of the layer steadily increased to about 312m by 2012 and then ultimately decreased in size to approximately 150m by 2017 (Fig. S36). $PreNO_3$ inside the negative $PreNO_3$ layer stayed relatively constant around -0.6µM between 2009 and 2011 and was the most negative in 2012, -0.98µM (Fig. S36). $PreNO_3$ inside the negative $PreNO_3$ layer then became less negative where it was -0.43µM by 2017 (Fig. S36). The yearly average of ocean temperature after 2007 decreased to 19.33 ˚C by 2012, increased again between 2013 and 2015 with a maximum value of 20.29 ˚C, and then decreased again to 17.19 ˚C by 2017 (Fig. S36).

CHAPTER III

DISCUSSION

The general observation of swapping between negative $PreNO_3$ anomalies in the winter and positive $PreNO_3$ anomalies for the rest of the year in the upper 100m is likely due to winter vertical mixing redistributing the subsurface negative $PreNO_3$ anomaly signal when bringing nutrients up from depth (Fig. 4, 5, 6). The fact that EQPACW 8474 and 12788 did overlap spatially and temporally at one point, but showed differences in their $PreNO_3$ observations is likely the result of the profiling floats following different water parcels and is unlikely due to

sensor error (Fig. S18, S22). The years 2015 and 2016 both experienced a strong El Niño period which corresponds to the years that the Bio-Argo floats in the North Pacific recorded the largest negative $PreNO_3$ subsurface layer (Fig. S36; Shea, 2018). The anomalous warming of the North Pacific known as 'the Blob' that occurred from the years 2013 to 2015, can be seen in the interannual variability of temperature (Fig. S36; Siedlecki et al. 2016). The thickness of the negative $PreNO_3$ subsurface layer increased and the $PreNO_3$ values became more negative from 2013 to 2015, which potentially could be attributed to the Blob or the transition to a strong El Niño (Fig. S36).

Table 3. Mean positive and negative rates of $PreNO_3$ anomaly formation within 25m to 75m, the middle, and bottom layer where regression were performed for each regional group based on Bio-Argo float name or area that they primarily took observations in.

Region	25m to 75m Mean Positive $PreNO_3$ Rate ($\frac{\mu mol\ N}{m^3\ day}$)	25m to 75m Mean Negative $PreNO_3$ Rate ($\frac{\mu mol\ N}{m^3\ day}$)	Middle Layer Mean Positive $PreNO_3$ Rate ($\frac{\mu mol\ N}{m^3\ day}$)	Middle Layer Mean Negative $PreNO_3$ Rate ($\frac{\mu mol\ N}{m^3\ day}$)	Bottom Layer Mean Positive $PreNO_3$ Rate ($\frac{\mu mol\ N}{m^3\ day}$)	Bottom Layer Mean Negative $PreNO_3$ Rate ($\frac{\mu mol\ N}{m^3\ day}$)
Hawaii	3.92	-4.30	3.14	-2.54	2.22	-2.48
Bermuda	10.05	-5.94	12.49	-11.68	11.18	-8.50
California Current	8.68	-10.84	7.40	-6.83	9.56	-20.30
Easter Tropical North Pacific	3.57	-7.28	5.12	-11.53	15.87	-17.41
East Tropical South Pacific	2.30	-4.13	2.37	-2.88	7.45	-4.23
Kuroshio Current	12.49	-14.70	13.03	-7.72	10.88	-7.74
Equatorial West Pacific	8.24	-6.26	17.62	-2.43	11.23	-29.91

The equivalence of the absolute value of euphotic zone positive rates of $PreNO_3$ anomaly formation compared to the absolute value of subsurface negative rates of $PreNO_3$ anomaly formation, can speak to if all anomaly generating processes are being accounted for or if there are processes missing (Table. 3). In Hawaii, Bermuda, California Current, and the ETSP absolute values for euphotic zone positive rates of $PreNO_3$ anomaly formation are roughly equivalent to the absolute value of the negative rates within the subsurface layers (Table. 3). This suggests that whatever process is causing anomalies in the euphotic zone is related to the process that is

causing anomalies in the subsurface layers for Hawaii, Bermuda, California Current, and the ETSP (Table. 3). However this is not the case for the other floats groups, suggesting that in these other regions there are anomaly generating process that are not being accounted for (Table. 3). Note that the values for the East Tropical South Pacific (ETSP) are the same as the values for SOPACIFIC 7553 in Table. 2, because SOPACIFIC 7553 was the only float that took observations in the ETSP (Table. 3). The rates of $PreNO_3$ anomaly formation reported for Station ALOHA from Letscher & Villareal, 2018 agree with those reported in Table. 3, however the rates for BATS in Table. 3 are greater than those from Letscher & Villareal, 2018.

Vertically Migrating Phytoplankton & Transparent Exopolymer Particles

The TEP mechanism involves net community production at the surface of N-deficient polysaccharides forming positive $PreNO_3$ anomalies and then subsequently aggregate and sink out of the euphotic zone where it is remineralized forming negative $PreNO_3$ anomalies (Fig. 1). The VMP mechanism involves descending to consume nitrate which forms negative $PreNO_3$ anomalies and then ascending to the surface to photosynthesize forming positive $PreNO_3$ anomalies (Fig. 1). The mechanism responsible for the formation of positive and negative $PreNO_3$ anomalies could be determined based on the timing of euphotic positive $PreNO_3$ anomalies compared to the timing of sub-euphotic zone negative $PreNO_3$ anomalies. TEP may only sink a few meters per year whereas VMP can migrate tens of meter in just a day (Fig. 1; Mari et al. 2017; Letscher & Villareal, 2018; Wirtz & Smith, 2020). It is worth noting that TEP can act as the glue for marine snow allowing for the sinking speed of TEP when attached to marine snow particles to be much faster than when TEP is on its own (Asper 1987; Passow 2002; Busch et al. 2017). Therefore due to the differences in their sinking/migrating speeds, if euphotic zone positive $PreNO_3$ anomalies occur at relatively the same time as sub-euphotic zone negative

$PreNO_3$ anomalies in the monthly smoothed estimates of $PreNO_3$ then VMP could be the responsible $PreNO_3$ anomaly generating biogeochemical process. Whereas if euphotic zone positive $PreNO_3$ anomalies occur before (weeks to months) sub-euphotic zone negative $PreNO_3$ anomalies then TEP could be the responsible anomaly generating process since the TEP pool must accumulate slowly following the production of dissolved carbohydrate precursors as a product of net community production in the euphotic zone before it becomes negatively buoyant and starts slowly sinking (Mari et al. 2017; Letscher & Villareal, 2018).

North Pacific

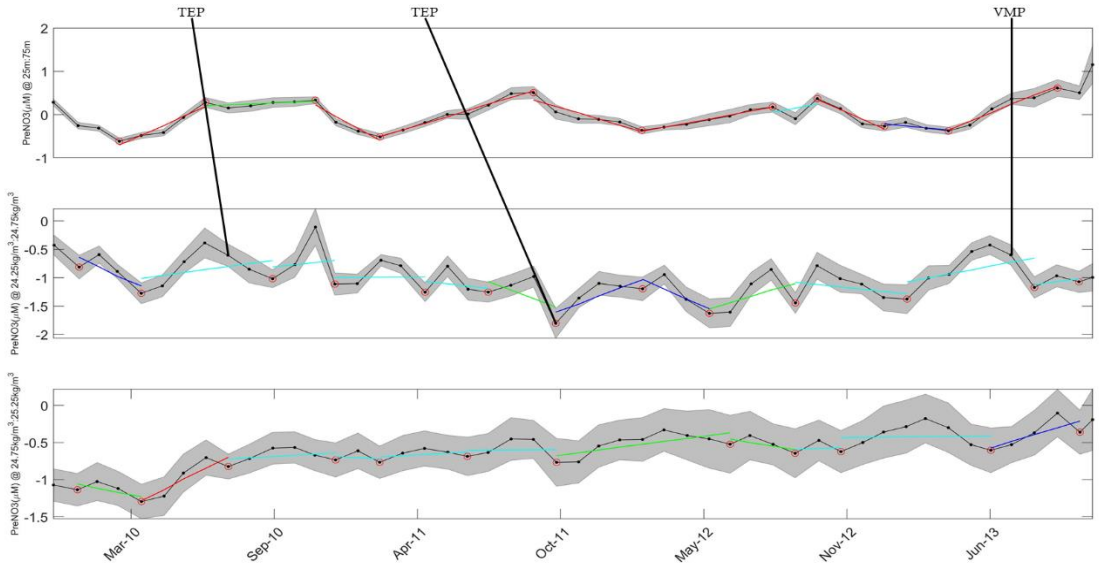

Figure 13. $PreNO_3$ for Hawaii 6401 smoothed to show $PreNO_3$ per month with regression of $PreNO_3$ vs time. Top figure $PreNO_3$ at 25m-75m, middle figure $PreNO_3$ at 24.5$\frac{kg}{m^3}$:24.9$\frac{kg}{m^3}$, and bottom figure $PreNO_3$ at 24.9$\frac{kg}{m^3}$:25.3$\frac{kg}{m^3}$. Black dots are observations and the ones with red circles are local minima and maxima. Regressions colored by the value of the correlation coefficient; r^2>0.75(Red), 0.75> r^2>0.5(Blue), 0.5> r^2>0.25(Green), 0.25> r^2>0(Cyan). Grey regions represent 95% confidence intervals for $PreNO_3$ values. Black lines on figures indicate observations where TEP or VMP may have been responsible.

South Pacific

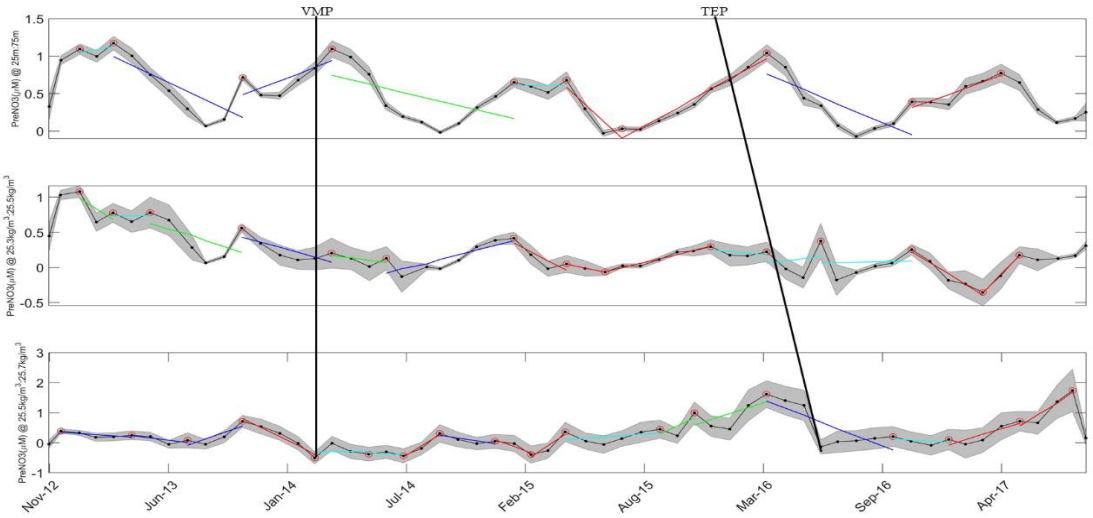

Figure 14. $PreNO_3$ for SOPACIFIC 7553 smoothed to show $PreNO_3$ per month with regression of $PreNO_3$ vs time. Top figure $PreNO_3$ at 25m-75m, middle figure $PreNO_3$ at 25.3$\frac{kg}{m^3}$:25.5$\frac{kg}{m^3}$, and bottom figure $PreNO_3$ at 25.5$\frac{kg}{m^3}$:25.7$\frac{kg}{m^3}$. Black dots are observations and the ones with red circles are local minima and maxima. Regressions colored by the value of the correlation coefficient; r^2>0.75(Red), 0.75> r^2>0.5(Blue), 0.5> r^2>0.25(Green), 0.25> r^2>0(Cyan). Grey regions represent 95% confidence intervals for $PreNO_3$ values. Black lines on figures indicate observations where TEP or VMP may have been responsible.

North Atlantic

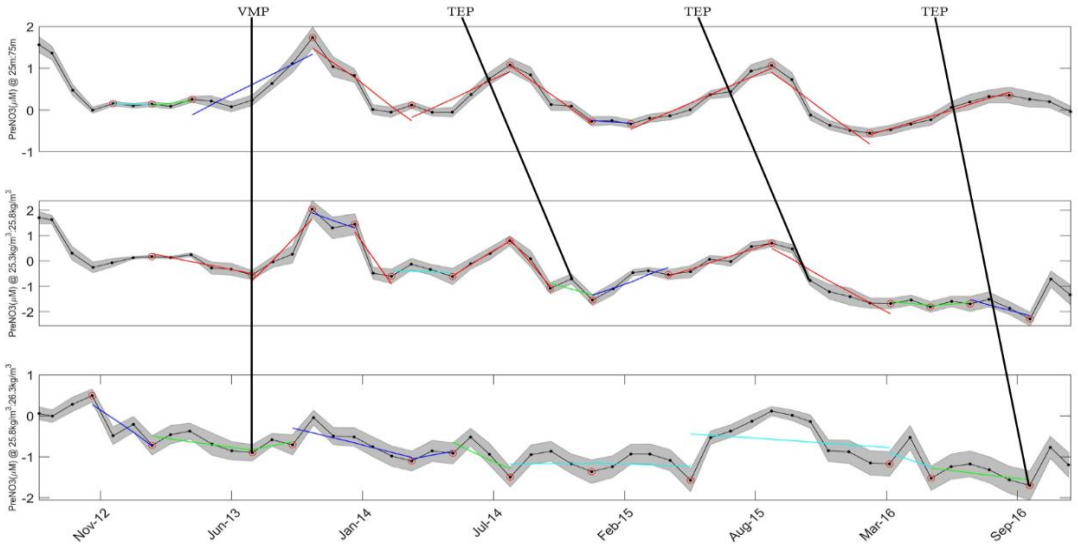

Figure 15. $PreNO_3$ for Bermuda 7663 smoothed to show $PreNO_3$ per month with regression of $PreNO_3$ vs time. Top figure $PreNO_3$ at 25m-75m, middle figure $PreNO_3$ at 25.3$\frac{kg}{m^3}$:25.8$\frac{kg}{m^3}$, and bottom figure $PreNO_3$ at 25.8$\frac{kg}{m^3}$:26.3$\frac{kg}{m^3}$. Black dots are observations and the ones with red circles are local minima and maxima. Regressions colored by the value of the correlation coefficient; r^2>0.75(Red), 0.75> r^2>0.5(Blue), 0.5> r^2>0.25(Green), 0.25> r^2>0(Cyan). Grey regions represent 95% confidence intervals for $PreNO_3$ values. Black lines on figures indicate observations where TEP or VMP may have been responsible.

Whether TEP or VMP was responsible for $PreNO_3$ anomalies could be determined by comparing the timing of euphotic positive $PreNO_3$ anomalies and the timing of sub-euphotic zone negative $PreNO_3$ anomalies. The profiling floats with patterns suggestive of only TEP being responsible for $PreNO_3$ anomalies were Bermuda 6976, CALCURRENT 7618, and KUROSHIO 7546 (Fig. S17, S19, S31). The only profiling float with patterns suggestive of VMP solely being responsible for the formation of $PreNO_3$ anomalies was EQPACW 8474 (Fig. S23). The profiling floats with patterns suggestive of $PreNO_3$ anomalies being formed by a combination of TEP and VMP were: Hawaii 6891, Hawaii 5145, Hawaii 6403, Hawaii 6401, Hawaii 8486, Hawaii 8497, Bermuda 7663, Bermuda 6975, Bermuda 6391, KUROSHIO 7674, ETNP 6960, ETNP 7558, and SOPACIFIC 7553 (Fig. S7, 7, S5, 13, S9, S11, 15, S15, S13, S33, S27, S29, 14). The profiling floats where it was not discernable what mechanism was responsible for the formation of $PreNO_3$ anomalies were: CALCURRENT 7647, NOPACIFIC 7642, and EQPACW 12788 (Fig. S21, S35, S25).

Identifying and quantifying the exact biogeochemical mechanism(s) driving the formation of $PreNO_3$ anomalies in the shallow subtropical ocean is an important goal in the face of the predicted expansion of the subtropical ocean biome in the 21st century (Polovina et al. 2008). Since most known vertical migrator phytoplankton are diatoms (Villareal et al. 2014), the VMP mechanism could be an efficient transporter of carbon as a result of their shells acting as mineral ballasts. The overall magnitude of the ocean's biological carbon pump, currently estimated at 12±2 Pg C yr^{-1} (Emerson 2014), is predicted to decline over the 21st century as the expansion of the subtropical marine biome displaces adjacent higher nutrient biomes preferentially populated with diatoms and other efficient carbon exporters including calcifiers. However, if VMP was to be determined to be the primary driver of $PreNO_3$ anomaly formation in

the shallow subtropics then this predicted expansion of the subtropical ocean may not result in a decrease in the oceans biological pump since diatoms can be continually sustained via the VMP mechanism. Whereas if TEP were to be determined to be the primary driver of $PreNO_3$ anomaly formation then the predicted expansion of the subtropical ocean could induce a less efficient biological carbon pump. TEP exhibits slow sinking speeds (order meters per year) and some observations suggest that only a small percent of TEP will attain sufficient density to actually sink out of surface waters (Mari et al. 2017). The DIC produced by the consumption of TEP is recycled within the shallow seasonal thermocline and is in contact with the atmosphere on annual timescales, thus contributing little to the oceans biological carbon pump or carbon sequestration.

Table 4. Number of occurrences of either TEP or VMP events observed in each regional group based on Bio-Argo float name or area that they primarily took observations in.

Region	TEP	VMP
Hawaii	13	11
Bermuda	8	3
California Current	4	0
East Tropical North Pacific	4	2
East Tropical South Pacific	1	1
Kuroshio Current	3	1
Equatorial West Pacific	0	1

Events of both TEP and VMP causing the formation of $PreNO_3$ anomalies were observed the most around Hawaii (Table. 4). However it seems that both VMP and TEP are equally important in causing the formation of $PreNO_3$ anomalies around Hawaii, ETNP, ETSP where SOPACIFIC 7553 was, and the Kuroshio Current (Table. 4). TEP seems to be the more important mechanism around Bermuda (Table. 4). There is not enough evidence to determine which mechanism is more important in the EQPACW and the California Current (Table. 4). Four out of the five Bio-Argo floats used in Fawcett et al. 2018 was used for this research; Bermuda 7663, Bermuda 6391, Bermuda 6975, and Bermuda 6976 (Fig. 6, 15, S12:S17). Observations of

the occurrence of TEP causing the formation of $PreNO_3$ anomalies from; Bermuda 7663, Bermuda 6975, Bermuda 6976, and Bermuda 6391 agree with the suggestion by Fawcett et al. 2018 that the remineralization of TEP is most likely responsible for $PreNO_3$ anomaly formation (Fig. 15, S13, S15, S17). However VMP events were still observed in the $PreNO_3$ records of; Bermuda 7663, Bermuda 6975, and Bermuda 6391 (Fig. 15, S13, S15). Hawaii 5145 is the same float that was used in Johnson et al. 2010 and the observation of one VMP event in the $PreNO_3$ records of Hawaii 5145 agrees with the suggestion that VMP is the most likely mechanism for $PreNO_3$ anomaly formation (Fig. 7).

Taxa of VMP (*Pyrocystis*, *Ethmodiscus*, *Rhizosolenia*) are more abundant in the Pacific Ocean then the Atlantic Ocean (Letscher & Villareal, 2018). Since the depths of the core of positive $PreNO_3$ anomalies does not agree with changes in AOU around Hawaii as well as it does around Bermuda, something else besides VMP could be causing euphotic zone positive $PreNO_3$ anomalies around Hawaii (Fig. 12). The monthly averages of the depths of the core of the negative $PreNO_3$ anomaly layers track the seasonal changes in the euphotic zone, since the depths of the core of the negative $PreNO_3$ anomaly layers is deepest in the summer and shallowest in winter (Fig. 12). This can also be seen in the seasonality of the distribution of negative $PreNO_3$ anomalies, where negative $PreNO_3$ anomalies generally descend below 100m in summer and then ascend again in the winter (Fig. 10, 11). There isn't much seasonal variability for the depth of the core of positive $PreNO_3$ anomaly layers around Hawaii and Bermuda, (change of only a few meters) (Fig. 12).

Thirteen out of the twenty Bio-Argo floats that were examined indicate that positive euphotic zone, and negative subsurface $PreNO_3$ anomalies were likely the result of a combination of both the VMP and TEP mechanisms (Fig. S7, 7, S5, 13, S9, S11, 15, S15, S13, S33, S27, S29,

14). Three out of the twenty Bio-Argo floats examined indicate that positive euphotic zone, and negative subsurface $PreNO_3$ anomalies were likely solely the result of the TEP mechanism (Fig. S17, S19, S31). Whereas only one out of the twenty Bio-Argo floats that were examined indicated that positive euphotic zone, and negative subsurface $PreNO_3$ anomalies were likely caused by the VMP mechanism alone (Fig. S23). Out of the twenty Bio-Argo floats examined, VMP was identified 17 times whereas TEP was identified 33 times as the mechanisms driving $PreNO_3$ anomaly formation, thus it seems that TEP occurred nearly twice as much in the Bio-Argo float record over the years 2007:2019. However, we are unable to quantify the importance of each mechanism to the overall rate of $PreNO_3$ anomaly formation. Such analysis requires more information not easily gleaned from the extant Bio-Argo suite, e.g. migrator phytoplankton biomass and TEP quantity and carbon content. Identifying the mechanisms of $PreNO_3$ anomaly formation is important in understanding the true stoichiometry of biochemical reactions as well as better understanding the biological pump.

CHAPTER IV

CONCLUSIONS

Solving the mystery of the biogeochemical processes responsible for the generation of $PreNO_3$ anomalies that oceanographers have been investigating for decades will give insight into non-Redfield processes that accounts for changes in oxygen without stoichiometric changes in nitrate. Bio-Argo floats provide the opportunity to get high resolution observations of biogeochemical processes which can help find answers to many oceanographic questions such as what mechanisms drive the formation of $PreNO_3$ anomalies. Analyses have shown that both euphotic zone positive and subsurface negative $PreNO_3$ anomalies are widespread in the subtropical ocean and while there is some variability in the $PreNO_3$ values and sign, these vertically segregated $PreNO_3$ anomalies are persistent seasonally in the Bio-Argo $PreNO_3$ record.

However due to the amount of time Bio-Argo floats spend at 1000m depth (~9.5 days) there could be significant spatial differences between the water masses that Bio-Argo floats descend in and the water masses that they eventually ascend in (Claustre et al. 2019). $PreNO_3$ anomalies being wide spread in the subtropical ocean suggests that they could have a strong influence on the biological pump that is thus far not included in global estimates of the ocean's biological pump as estimated by the current class of Earth System Models (e.g. Moore et al. 2018; Stock et al. 2020), ocean color based models (e.g. Westberry et al.2008; Silsbe et al. 2016), and particle flux models (DeVries et al. 2014; Cael and Bisson, 2018). The locations of $PreNO_3$ anomalies are consistent with previous observations of VMP taxa (*Pyrocystis, Ethmodiscus, Rhizosolenia*) throughout the global subtropical ocean (Fig. 10, 11; Letscher & Villareal, 2018, Figures S11-13). The timing of euphotic zone positive $PreNO_3$ anomalies in relation to sub-euphotic zone negative $PreNO_3$ anomalies suggest that both the export and remineralization of TEP as well as the utilization of stocks of nitrate by VMP play roles in the formation of $PreNO_3$ anomalies. Further investigation of both TEP and VMP including abundance and stoichiometry is needed to better understand the formation of $PreNO_3$ anomalies as well as the influence $PreNO_3$ anomalies may have on ocean biogeochemistry into the future.

LIST OF REFERNCES

Abell, Jeffrey, Steve Emerson, and Richard G. Keil, 2005, Using preformed nitrate to infer decadal changes in DOM remineralization in the subtropical North Pacific, GLOBAL BIOGEOCHEMICAL CYCLES, v. 19, doi:10.1029/2004GB002285.

Alldredge, Alice L., Uta Passow, and Bruce E. Logan, 1993, The abundance and significance of a class of large, transparent organic particles in the ocean, Deep-Sea Research I, v. 40, p.1131-1140.

Asper, Vernon L., 1987, Measuring the flux and sinking speed of marine snow aggregates, Deep-Sea Research, v.34, p.1-17, https://doi.org/10.1016/0198-0149(87)90117-8.

Busch, Kathrin, Sonja Endres, Morten H. Iversen, Jan Michels, Eva-Maria Nothig, and Anja Engel, 2017, Bacterial Colonization and Vertical Distribution of Marine Gel Particles (TEP and CSP) in the Arctic Fram Strait, Frontiers in Marine Science, v.4, doi: 10.3389/fmars.2017.00166

Broecker, Wallace S., 1974, "NO", A CONSERVATIVE WATER-MASS TRACER*, Earth and Planetary Science Letters, v.23, p.100-107.

Cael, B. B., and Kelsey Bisson, 2018, Particle Flux Parameterizations: Quantitative and Mechanistic Similarities and Differences, Frontiers in Marine Science, v.5, doi: 10.3389/fmars.2018.00395.

Cisternas-Novoa, Carolina, Cindy Lee, and Anja Engel, 2015, Transparent exopolymer particles (TEP) and Coomassie stainable particles (CSP): Differences between their origin and vertical distributions in the ocean, Marine Chemistry, v.175, p. 56-71.

Claustre, Herve, Kenneth S. Johnson, and Yuichiro Takeshita, 2019, Observing the Global Ocean with Biogeochemical-Argo, Annual Review of Marine Science, v.12, p.23-48, https://doi.org/10.1146/annurev-marine-010419-010956.

DeVries, T., J.-H. Liang, and C. Deutsch, 2014, A mechanistic particle flux model applied to the oceanic phosphorus cycle, Biogeosciences, v.11, p. 5381-5398, doi:10.5194/bg-11-5381-2014.

Emerson, Steven, 2014, Annual net community production and the biological carbon flux in the ocean, Global Biogeochemical Cycles, v. 28, p.1-12, doi:10.1002/2013GB004680.

Emerson, Steven, and Thomas L. Hayward, 1995, Chemical tracers of biological processes in shallow waters of North Pacific: Preformed nitrate distributions, Journal of Marine Research, v.53, p.499-513.

Engel, Anja, 2003, Distribution of transparent exopolymer particles (TEP) in the northeast Atlantic Ocean and their potential significance for aggregation processes, Deep Sea Research Part I, v.51, p. 83-92, doi:10.1016/j.dsr.2003.09.001.

Fawcett, Sarah E., Kenneth S. Johnson, Stephen C. Riser, Nicolas Van Oostende, Daniel M. Sigman, 2018, Low-nutrient organic matter in the Sargasso Sea thermocline: A

hypothesis for its role, identity, and carbon cycle implications, Marine Chemistry, https://doi.org/10.1016/j.marchem.2018.10.008.

Garcia, H. E., K. Weathers, C. R. Paver, I. Smolyar, T. P. Boyer, R. A. Locarnini, M. M. Zweng, A. V. Mishonov, O. K. Baranova, D. Seidov, and J. R. Reagan, 2018. *World Ocean Atlas 2018, Volume 3: Dissolved Oxygen, Apparent Oxygen Utilization, and Oxygen Saturation.* A. Mishonov Technical Ed.; NOAA Atlas NESDIS 83, 38 pp.

Garcia, H. E., K. Weathers, C. R. Paver, I. Smolyar, T. P. Boyer, R. A. Locarnini, M. M. Zweng, A. V. Mishonov, O. K. Baranova, D. Seidov, and J. R. Reagan, 2018. *World Ocean Atlas 2018, Volume 4: Dissolved Inorganic Nutrients (phosphate, nitrate and nitrate+nitrite, silicate).* A. Mishonov Technical Ed.; NOAA Atlas NESDIS 84, 35 pp.

Gruber, Nicolas, 2008, The Marine Nitrogen Cycle: Overview and Challenges, Nitrogen in the Marine Environment II, p.1-50.

Johnson, Kenneth S., Stephen C. Riser, and David M. Karl, 2010, Nitrate supply from deep to near-surface water of the North Pacific subtropical gyre, Nature Letters, v.465, p.1062-1065.

Letscher, Robert T., and Tracey A. Villareal, 2018, Evaluation of the seasonal formation of subsurface negative preformed nitrate anomalies in the subtropical North Pacific and North Atlantic, Biogeosciences, v.15, p.6461-6480.

Mari, Xavier, Uta Passsow, Christophe Migon, Adrian B. Burd, and Louis Legendre, 2017, Transparent exopolymer particles: Effects on carbon cycling in the ocean, Progress in Oceanography, v. 151, p. 13-37. https://doi.org/10.1016/j.pocean.2016.11.002.

MBARI, 2017, FloatViz 6.0 - Apex/ISUS Data Visualization, mbari.org, https://www.mbari.org/science/upper-ocean-systems/chemical-sensor-group/floatviz/.

Moran, Xose Anxelu G., Marta Sebastian, Carlos Pedros-Alio, and Marta Estrada, 2006, Response of Southern Ocean phytoplankton and bacterioplankton production to short term experimental warming, Limnology and Oceanography, v. 51, p. 1791-1800.

Moore, Keith J., Weiwei Fu, Francois Primeau, Gregory L. Britten, Keith Lindsay, Matthew Long, Scott C. Doney, Natalie Mahowald, Forrest Hoffman, James T. Randerson, 2018, Sustained climate warming drives declining marine biological productivity, Science, v. 359, p. 1139-1143.

Myklestad, Sverre M., 1995, Release of extracellular products by phytoplankton with special emphasis on polysaccharides, The Science of the Total Environment, v. 165, p. 155-164.

Paulmier, A., I. Kriest, and A. Oschlies, 2009, Stoichiometries of remineralisation and denitrification in global biogeochemical ocean models, Biogeosciences, v. 6, p. 923-935.

Passow, U., 2002, Transparent exopolymer particles (TEP) in aquatic environments, Progress in Oceanography, v. 55, p. 287-333.

Peltzer, Edward T., 2007, Matlab scripts for oceanographic calculations: aou, Monterey Bay Aquarium Research Institute (MBARI).

Pilskaln, C.H., T.A. Villareal, M. Dennet, C. Darjangelo-Wood, and G. Meadows, 2005, High concentrations of marine snow and diatom algal mats in the North Pacific Subtropical Gyre: Implications for carbon and nitrogen cycles in the oligotrophic ocean, Deep Sea Research Part I, v. 52, p. 2315-2332.

Polovina, Jeffery J., John P. Dunne, Phoebe A. Woodworth, and Evan A. Howell, 2011, Projected expansion of the subtropical biome and contraction of the temperate and equatorial upwelling biomes in the North Pacific under global warming, ICES Journal of Marine Science, doi:10.1093/icesjms/fsq198.

Redfield, A. C., B.H Ketchum, and F.A. Richards, 1963, The influence of organisms on the composition of sea water, The sea, p. 26-77.

Rivkin, Richard B., Elijah Swift, William H. Biggley, and Mary A. Voytek, 1984, Growth and carbon uptake by natural populations of oceanic dinoflagellates *Pyrocystis noctiluca* and *Pyrocystis fusiformis*, Deep Sea Research Part A., v. 31, p. 353-367, https://doi.org/10.1016/0198-0149(84)90089-X.

Shea, Dennis, 2018, NINO SST INDICES (NINO 1+2, 3, 3.4, 4; ONI AND TNI), climatedataguide.ucar.edu, https://climatedataguide.ucar.edu/climate-data/nino-sst-indices-nino-12-3-34-4-oni-and-tni.

Siedlecki, Samantha, Eric Bjorkstedt, Richard Feely, Adrienne Sutton, Jessica Cross, and Jan Newton, 2016, Impacts of the Blob on the Northeast Pacific Ocean biogeochemistry and ecosystems, US CLIVAR VARIATIONS, v.14, p.7-12.

Silsbe, Greg M., Michael J. Behrenfeld, Kimberly H. Halsey, Allen J. Milligan, and Toby K. Westberry, 2016, The CAFE model: A net production model for global ocean phytoplankton, Global Biogeochemical Cycles, v. 30, p. 1756-1777, doi:10.1002/2016GB005521.

Stock, Charles A., John P. Dunne, Songmiao Fan, Paul Ginoux, Jasmin John, John P. Krasting, Charlotte Laaufkotter, Fabien Paulot, Niki Zadeh, 2020, Ocean Biogeochemistry in GFDL's Earth System Model 4.1 and its Response to Increasing Atmospheric CO_2, Journal of Advances in Modeling Earth Systems, doi: 10.1029/2019MS002043.

The MathWorks™, Inc., 2019, MATLAB R2019b, Natick, Massachusetts, United States.

Villareal, Tracy A., Cynthia H. Pilskaln, Joseph P. Montoya, and Mark Dennett, 2014, Upward nitrate transport by phytoplankton in oceanic waters: balancing nutrient budgets in oligotrophic seas, PeerJ, DOI 10.7717/peerj.302.

Villareal, Tracy A., Leanne Joseph, Mark A. Brzezinski, Rebecca F. Shipe, Fredric Lipschultz, and Mark A. Altabet, 1999, Biological and Chemical Characteristics of the Giant Diatom Ethmodiscus (Bacillariophyceae) in the Central North Pacific Gyre, Journal of Phycology, v. 35, p. 896-902, DOI: 10.1046/j.1529-8817.1999.3550896.x.

Villareal, Tracy A., Samantha Woods, J. Keith Moore, and Karen Culver-Rymsza, 1996, Vertical Migration of *Rhizosolenia* mats and their significance to NO_3^- fluxes in the central North Pacific gyre, Journal of Plankton Research, v. 18, p. 1103-1121.

Westberry, T., M. J. Behrenfeld, D. A. Siegel, and E. Boss, 2008, Carbon-based primary productivity modeling with vertically resolved photoacclimation, Global Biogeochemical Cycles, v.22, doi:10.1029/2007GB003078.

Wirtz, Kai, and S. Lan Smith, 2020, Vertical migration by bulk phytoplankton sustains biodiversity and nutrient input to the surface ocean, Nature Scientific Reports, v.10 (1142).

Wurl, Oliver, Lisa Miller, and Svein Vagle, 2011, Production and fate of transparent exopolymer particles in the ocean, Journal of Geophysical Research, v.116.

SUPPLEMENT

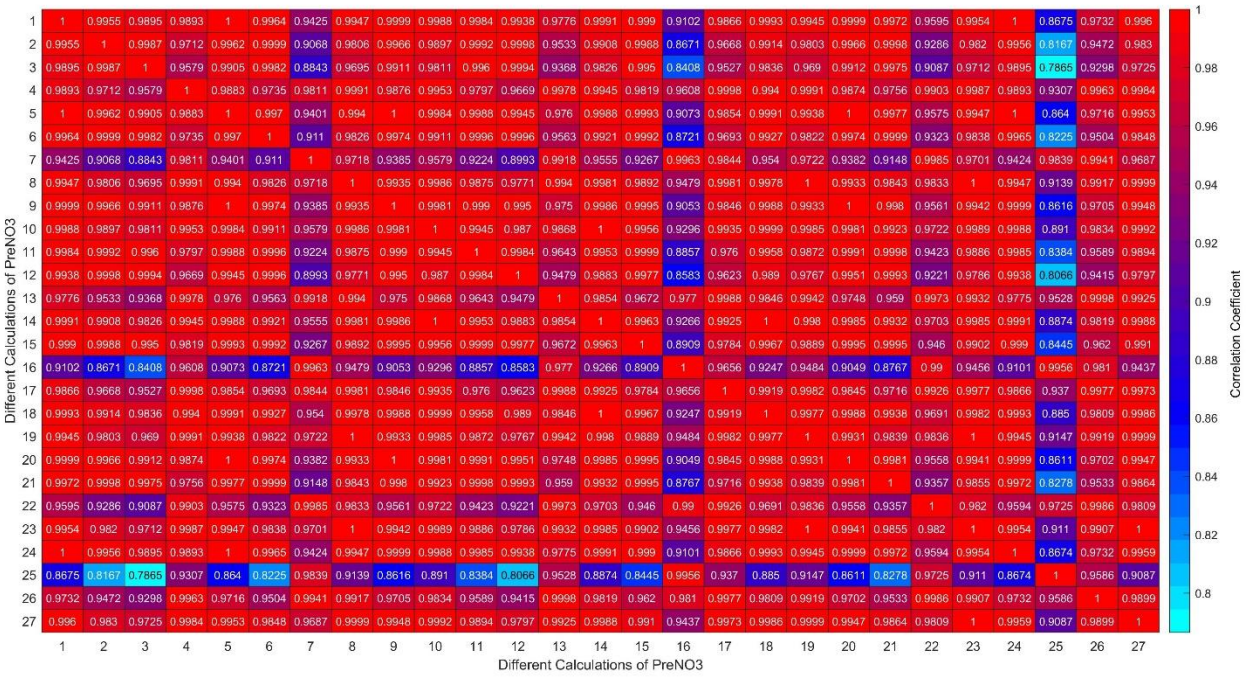

Figure S1. Correlations between 27 calculations of $PreNO_3$ for float, Hawaii 6401. Colorbar as well as values in boxes indicate the correlation between each different calculations of preformed nitrate.

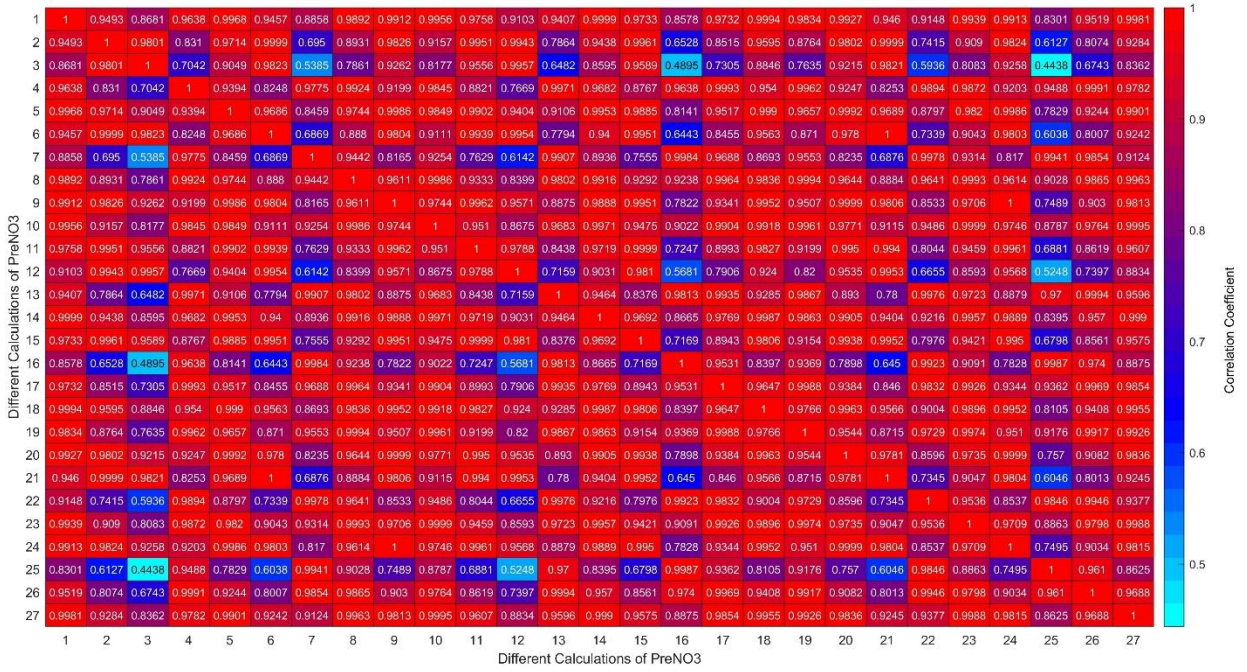

Figure S2. Correlations between 27 calculations of $PreNO_3$ for float, Bermuda 7663. Colorbar as well as values in boxes indicate the correlation between each different calculations of preformed nitrate.

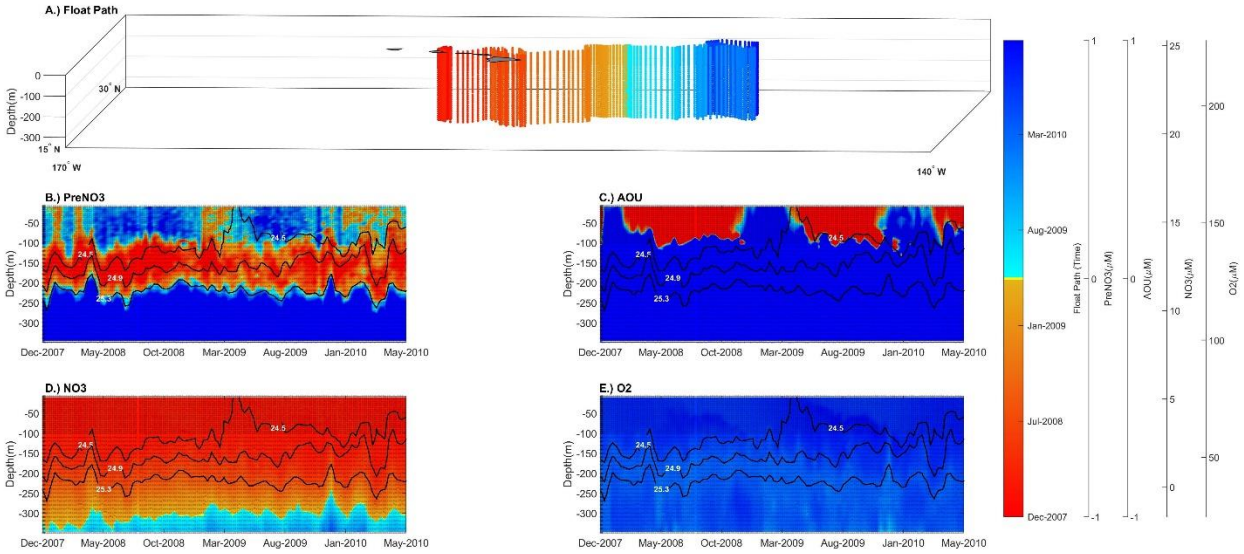

Figure S3. A.) Float path of Hawaii 5145 colored by time. B.) $PreNO_3$ for the first 350m of water column along float path from Dec-07 to Sep-10, C.) AOU for the first 350m of water column along float path. D.) NO_3 for the first 350m of water column along float path. E.) O_2 for the first 350m of water column along float path. Black lines in B:E represent isopycnals, 24.5$\frac{kg}{m^3}$, 24.9$\frac{kg}{m^3}$, and 25.3$\frac{kg}{m^3}$, chosen to outline anomalies. Dots in B:E represent observations. $PreNO_3$ and AOU limited to -1:1.

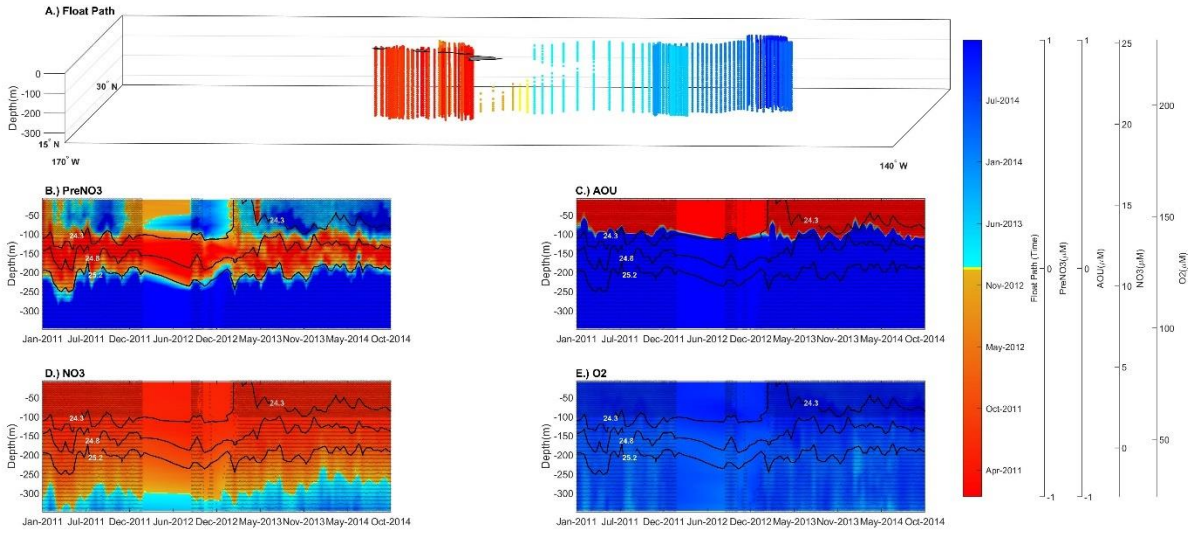

Figure S4. A.) Float path of Hawaii 6403 colored by time. B.) $PreNO_3$ for the first 350m of water column along float path from Jan-11 to Jan-15, C.) AOU for the first 350m of water column along float path. D.) NO_3 for the first 350m of water column along float path. E.) O_2 for the first 350m of water column along float path. Black lines in B:E represent isopycnals, 24.3$\frac{kg}{m^3}$, 24.8$\frac{kg}{m^3}$, and 25.2$\frac{kg}{m^3}$, chosen to outline anomalies. Dots in B:E represent observations. $PreNO_3$ and AOU limited to -1:1.

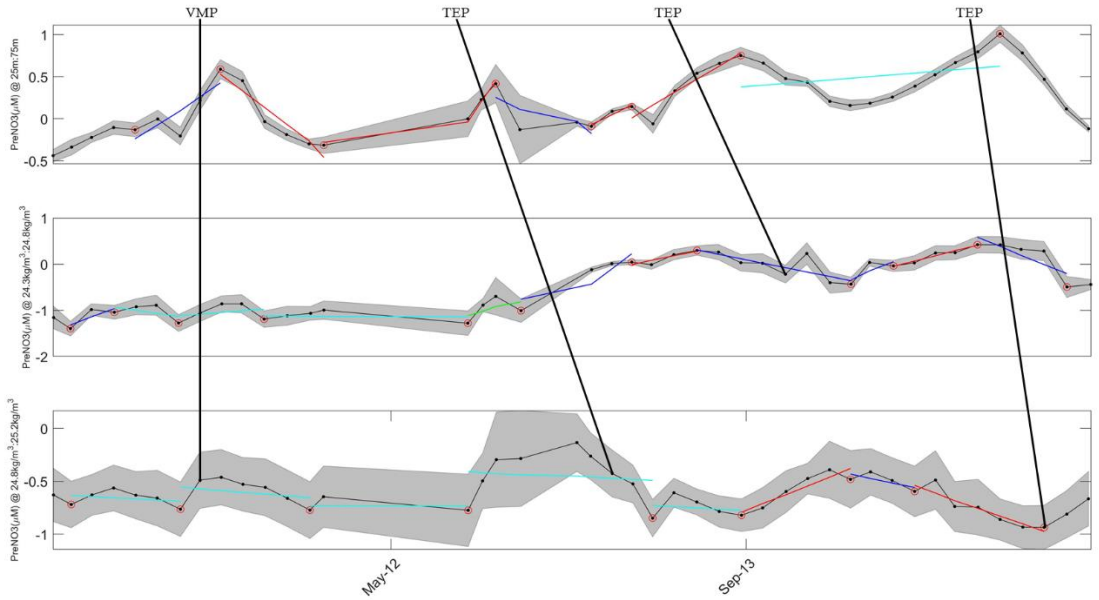

Figure S5. $PreNO_3$ for Hawaii 6403 smoothed to show $PreNO_3$ per month with regression of $PreNO_3$ vs time. Top figure $PreNO_3$ at 25m-75m, middle figure $PreNO_3$ at $24.3\frac{kg}{m^3}$:$24.8\frac{kg}{m^3}$, and bottom figure $PreNO_3$ at $24.8\frac{kg}{m^3}$:$25.2\frac{kg}{m^3}$. Black dots are observations and the ones with red circles are local minima and maxima. Regressions colored by the value of the correlation coefficient; r^2>0.75(Red), 0.75> r^2>0.5(Blue), 0.5> r^2>0.25(Green), 0.25> r^2>0(Cyan). Grey regions represent 95% confidence intervals for $PreNO_3$ values. Black lines on figures indicate observations where TEP or VMP may have been responsible.

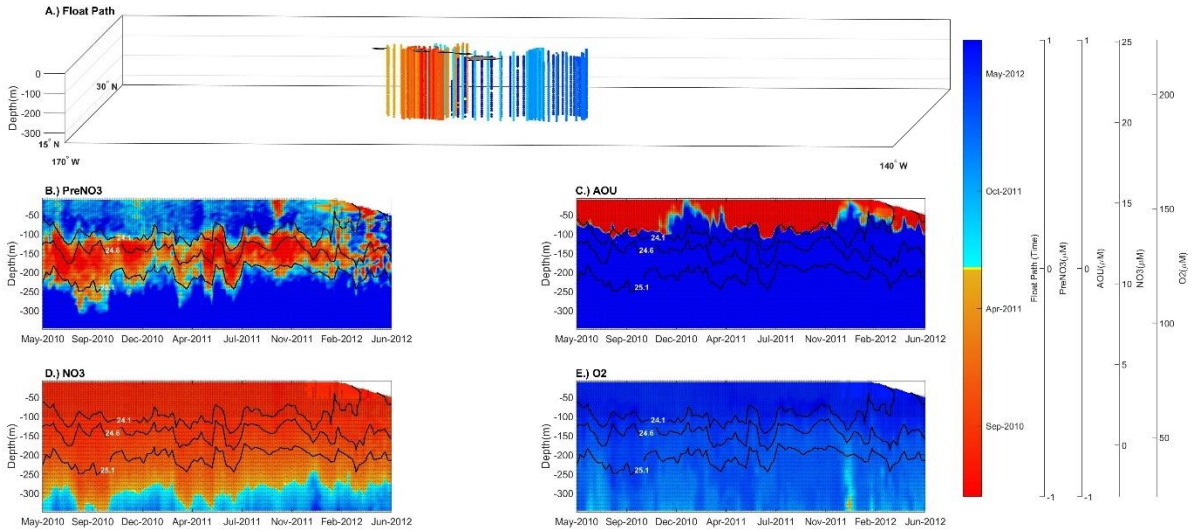

Figure S6. A.) Float path of Hawaii 6891 colored by time. B.) $PreNO_3$ for the first 350m of water column along float path from May-10 to Jul-12, C.) AOU for the first 350m of water column along float path. D.) NO_3 for the first 350m of water column along float path. E.) O_2 for the first 350m of water column along float path. Black lines in B:E represent isopycnals, $24.1\frac{kg}{m^3}$, $24.6\frac{kg}{m^3}$, and $25.1\frac{kg}{m^3}$, chosen to outline anomalies. Dots in B:E represent observations. $PreNO_3$ and AOU limited to -1:1.

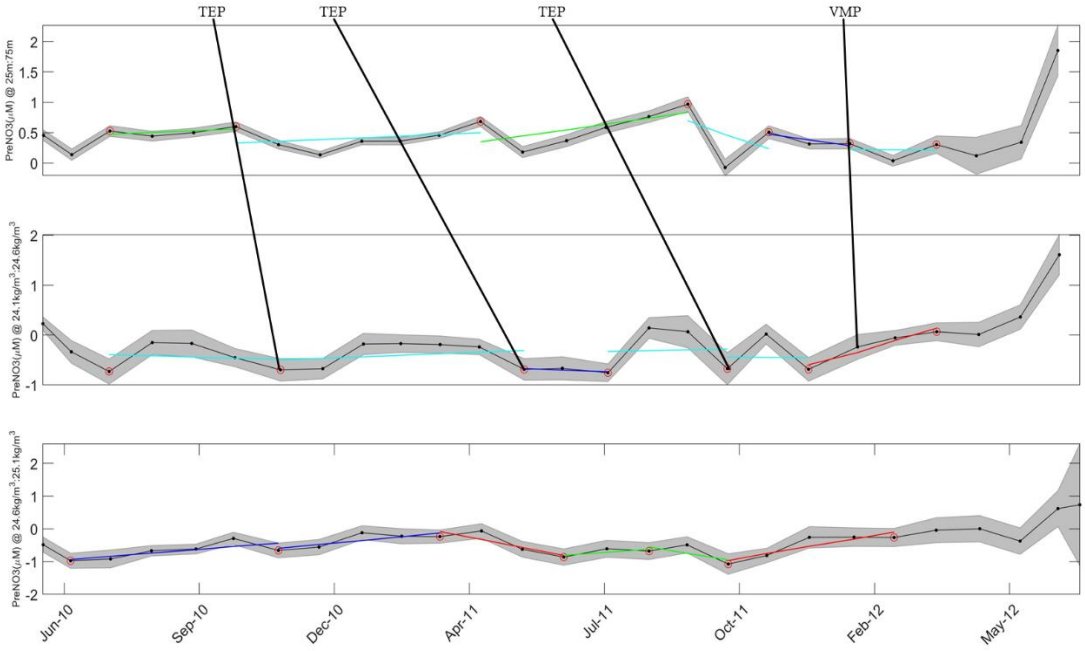

Figure S7. PreNO$_3$ for Hawaii 6891 smoothed to show PreNO$_3$ per month with regression of PreNO$_3$ vs time. Top figure PreNO$_3$ at 25m-75m, middle figure PreNO$_3$ at 24.1$\frac{kg}{m^3}$:24.6$\frac{kg}{m^3}$, and bottom figure PreNO$_3$ at 24.6$\frac{kg}{m^3}$:25.1$\frac{kg}{m^3}$. Black dots are observations and the ones with red circles are local minima and maxima. Regressions colored by the value of the correlation coefficient; r^2>0.75(Red), 0.75> r^2>0.5(Blue), 0.5> r^2>0.25(Green), 0.25> r^2>0(Cyan). Grey regions represent 95% confidence intervals for PreNO$_3$ values. Black lines on figures indicate observations where TEP or VMP may have been responsible.

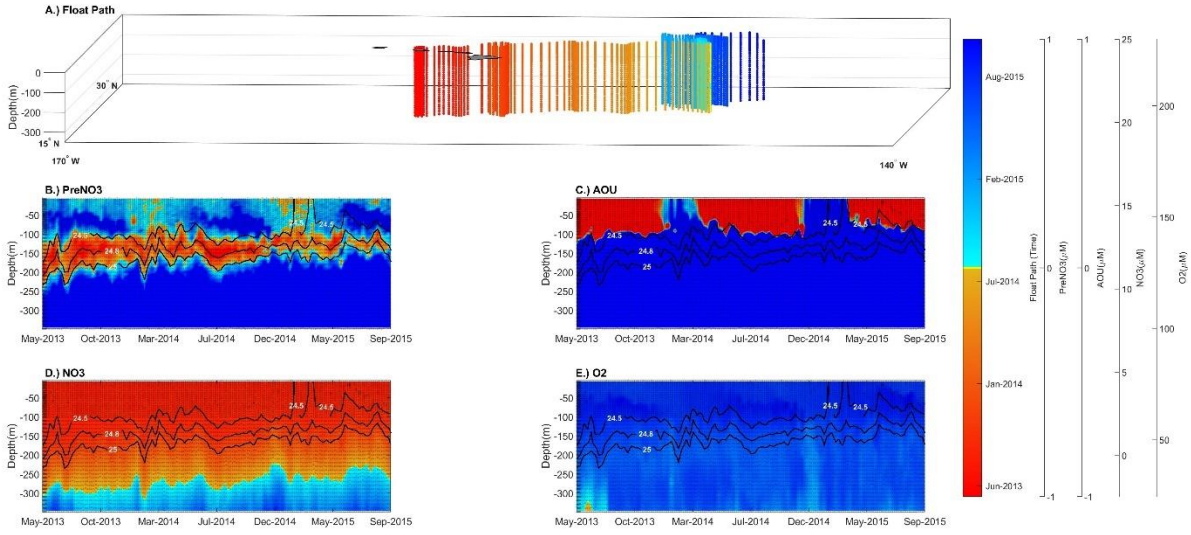

Figure S8. A.) Float path of Hawaii 8486 colored by time. B.) PreNO$_3$ for the first 350m of water column along float path from May-13 to Nov-15, C.) AOU for the first 350m of water column along float path. D.) NO$_3$ for the first 350m of water column along float path. E.) O$_2$ for the first 350m of water column along float path. Black lines in B:E represent isopycnals, 24.5$\frac{kg}{m^3}$, 24.8$\frac{kg}{m^3}$, and 25$\frac{kg}{m^3}$, chosen to outline anomalies. Dots in B:E represent observations. PreNO$_3$ and AOU limited to -1:1.

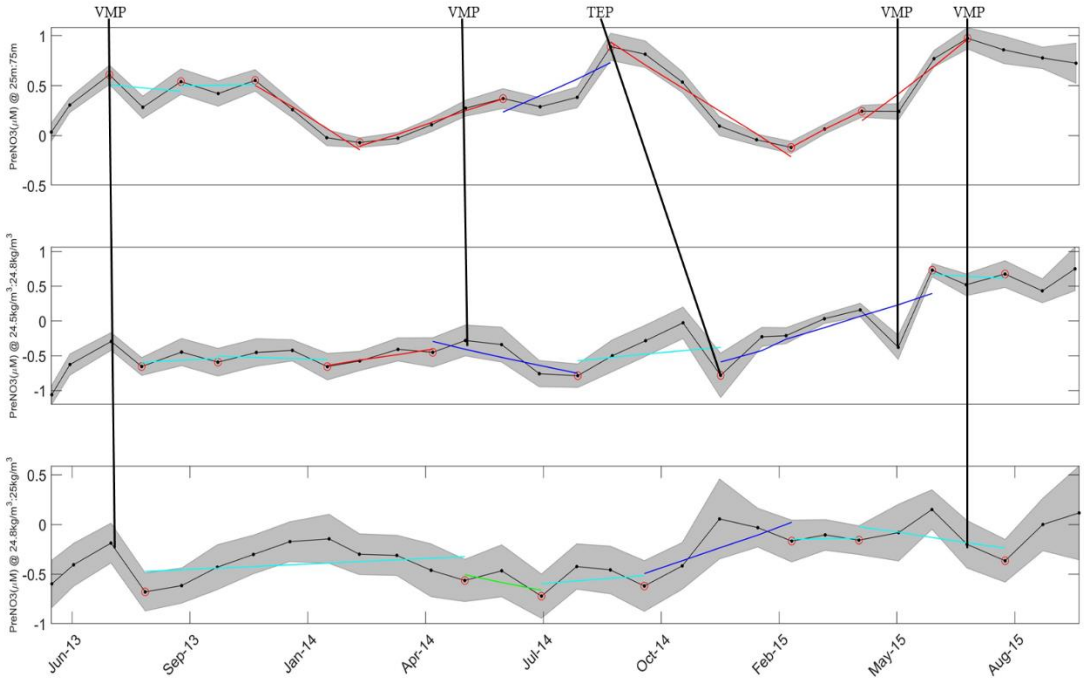

Figure S9. PreNO$_3$ for Hawaii 8486 smoothed to show PreNO$_3$ per month with regression of PreNO$_3$ vs time. Top figure PreNO$_3$ at 25m-75m, middle figure PreNO$_3$ at 24.5$\frac{kg}{m^3}$:24.8$\frac{kg}{m^3}$, and bottom figure PreNO$_3$ at 24.8$\frac{kg}{m^3}$:25$\frac{kg}{m^3}$. Black dots are observations and the ones with red circles are local minima and maxima. Regressions colored by the value of the correlation coefficient; r^2>0.75(Red), 0.75> r^2>0.5(Blue), 0.5> r^2>0.25(Green), 0.25> r^2>0(Cyan). Grey regions represent 95% confidence intervals for PreNO$_3$ values. Black lines on figures indicate observations where TEP or VMP may have been responsible.

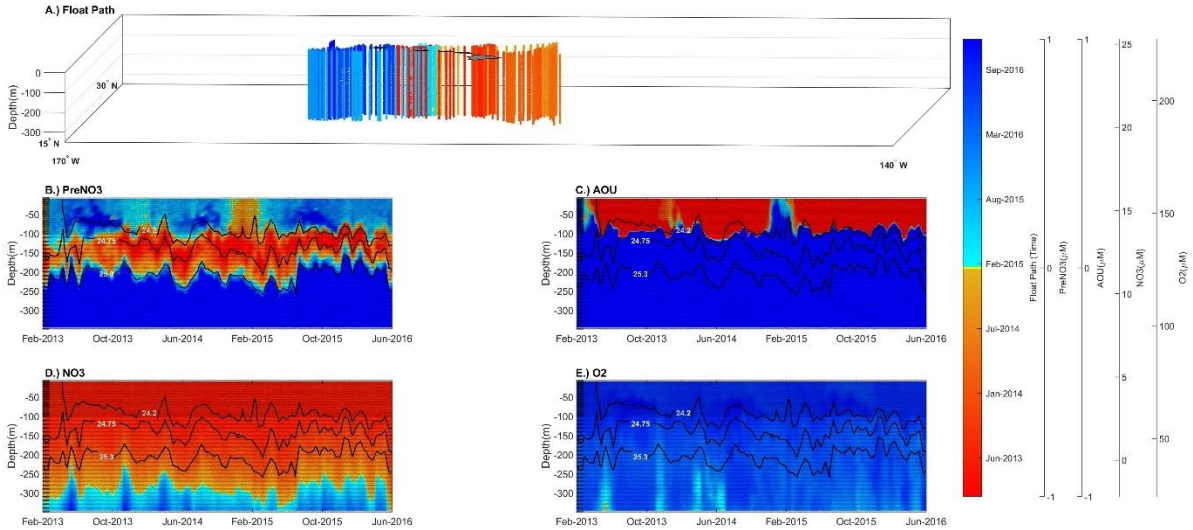

Figure S10. A.) Float path of Hawaii 8497 colored by time. B.) PreNO$_3$ for the first 350m of water column along float path from Feb-13 to Dec-16, C.) AOU for the first 350m of water column along float path. D.) NO$_3$ for the first 350m of water column along float path. E.) O$_2$ for the first 350m of water column along float path. Black lines in B:E represent isopycnals, 24.2$\frac{kg}{m^3}$, 24.75$\frac{kg}{m^3}$, and 25.3$\frac{kg}{m^3}$, chosen to outline anomalies. Dots in B:E represent observations. PreNO$_3$ and AOU limited to -1:1.

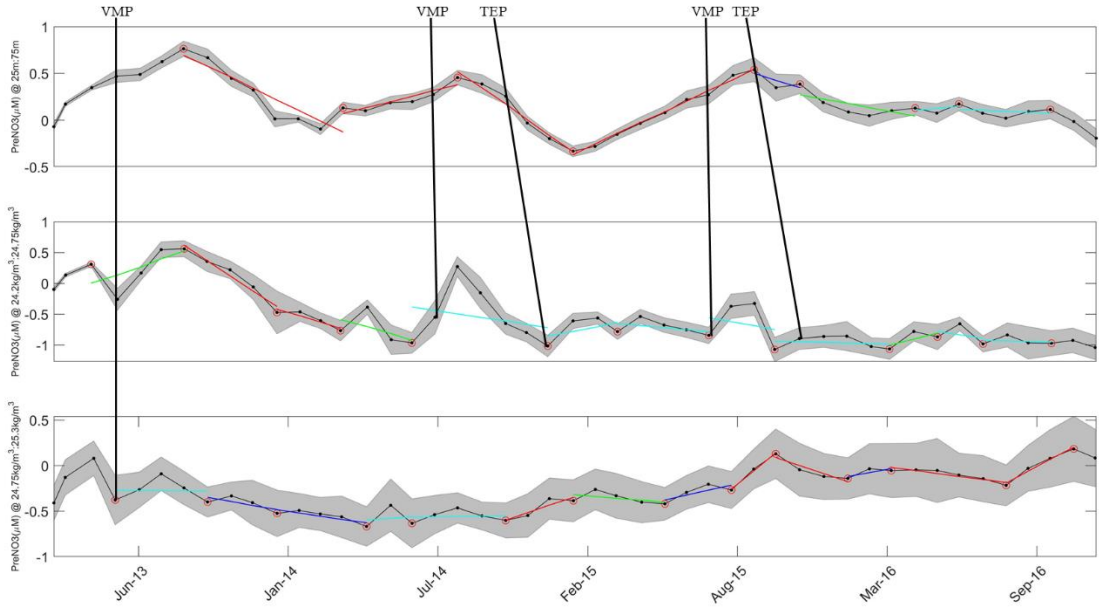

Figure S11. $PreNO_3$ for Hawaii 8497 smoothed to show $PreNO_3$ per month with regression of $PreNO_3$ vs time. Top figure $PreNO_3$ at 25m-75m, middle figure $PreNO_3$ at $24.2\frac{kg}{m^3}$:$24.75\frac{kg}{m^3}$, and bottom figure $PreNO_3$ at $24.75\frac{kg}{m^3}$:$25.3\frac{kg}{m^3}$. Black dots are observations and the ones with red circles are local minima and maxima. Regressions colored by the value of the correlation coefficient; r^2>0.75(Red), 0.75> r^2>0.5(Blue), 0.5> r^2>0.25(Green), 0.25> r^2>0(Cyan). Grey regions represent 95% confidence intervals for $PreNO_3$ values. Black lines on figures indicate observations where TEP or VMP may have been responsible.

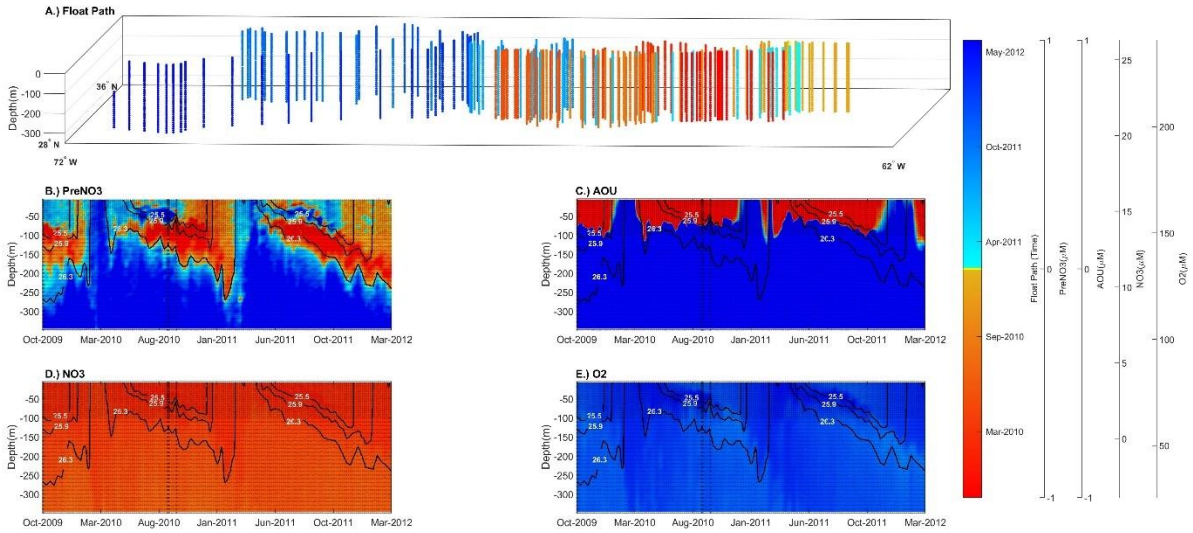

Figure S12. A.) Float path of Bermuda 6391 colored by time. B.) $PreNO_3$ for the first 350m of water column along float path from Oct-09 to Jun-12, C.) AOU for the first 350m of water column along float path. D.) NO_3 for the first 350m of water column along float path. E.) O_2 for the first 350m of water column along float path. Black lines in B:E represent isopycnals, $25.5\frac{kg}{m^3}$, $25.9\frac{kg}{m^3}$, and $26.3\frac{kg}{m^3}$, chosen to outline anomalies. Dots in B:E represent observations. $PreNO_3$ and AOU limited to -1:1.

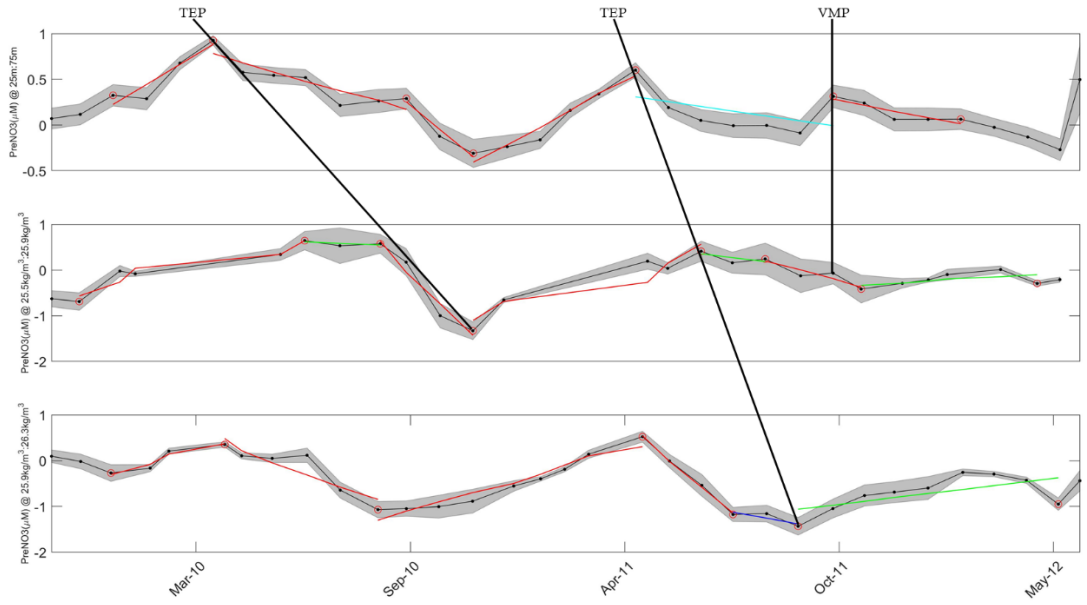

Figure S13. PreNO$_3$ for Bermuda 6391 smoothed to show PreNO$_3$ per month with regression of PreNO$_3$ vs time. Top figure PreNO3 at 25m-75m, middle figure PreNO$_3$ at 25.5$\frac{kg}{m^3}$: 25.9$\frac{kg}{m^3}$, and bottom figure PreNO$_3$ at 25.9$\frac{kg}{m^3}$:26.3$\frac{kg}{m^3}$. Black dots are observations and the ones with red circles are local minima and maxima. Regressions colored by the value of the correlation coefficient; r^2>0.75(Red), 0.75> r^2>0.5(Blue), 0.5> r^2>0.25(Green), 0.25> r^2>0(Cyan). Grey regions represent 95% confidence intervals for PreNO$_3$ values. Black lines on figures indicate observations where TEP or VMP may have been responsible.

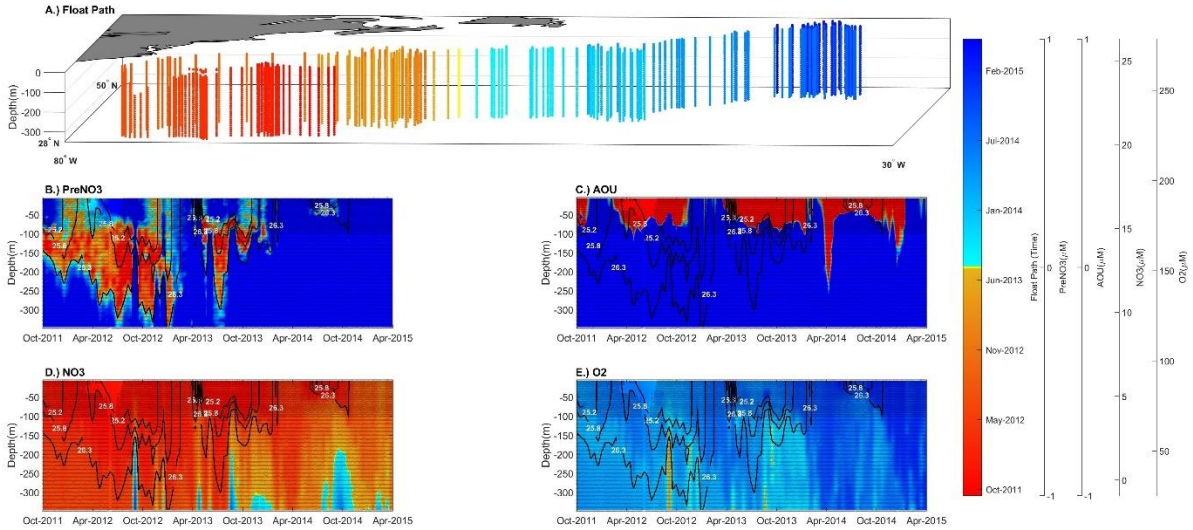

Figure S14. A.) Float path of Bermuda 6975 colored by time. B.) PreNO$_3$ for the first 350m of water column along float path from Oct-11 to May-15, C.) AOU for the first 350m of water column along float path. D.) NO$_3$ for the first 350m of water column along float path. E.) O$_2$ for the first 350m of water column along float path. Black lines in B:E represent isopycnals, 25.3$\frac{kg}{m^3}$, 25.8$\frac{kg}{m^3}$, and 26.3$\frac{kg}{m^3}$, chosen to outline anomalies. Dots in B:E represent observations. PreNO$_3$ and AOU limited to -1:1.

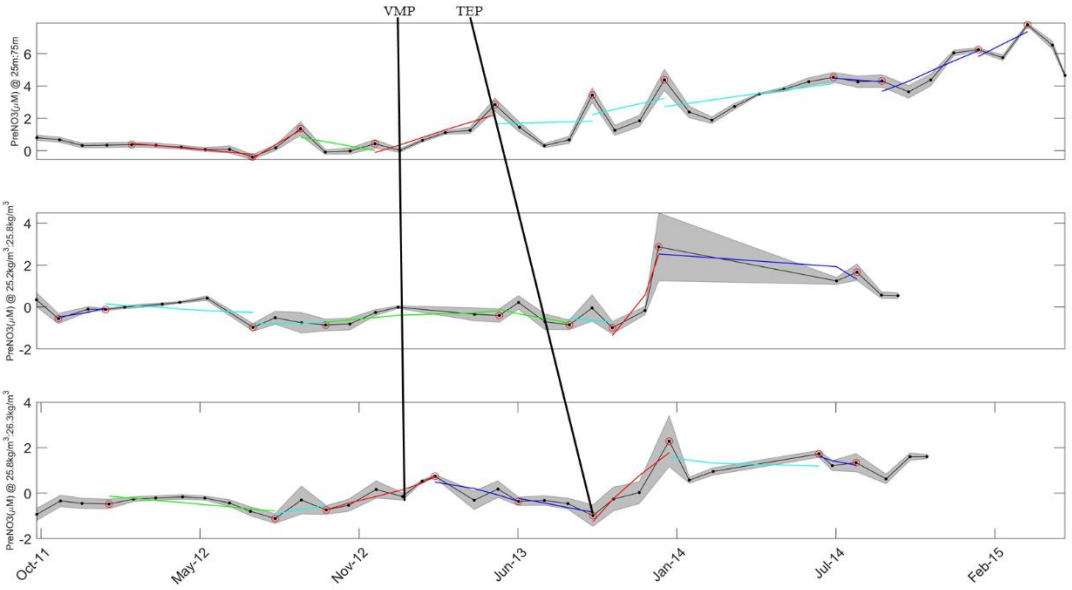

Figure S15. $PreNO_3$ for Bermuda 6975 smoothed to show $PreNO_3$ per month with regression of $PreNO_3$ vs time. Top figure PreNO3 at 25m-75m, middle figure $PreNO_3$ at 25.3$\frac{kg}{m^3}$: 25.8$\frac{kg}{m^3}$, and bottom figure $PreNO_3$ at 25.8$\frac{kg}{m^3}$:26.3$\frac{kg}{m^3}$. Black dots are observations and the ones with red circles are local minima and maxima. Regressions colored by the value of the correlation coefficient; r^2>0.75(Red), 0.75> r^2>0.5(Blue), 0.5> r^2>0.25(Green), 0.25> r^2>0(Cyan). Grey regions represent 95% confidence intervals for $PreNO_3$ values. Black lines on figures indicate observations where TEP or VMP may have been responsible.

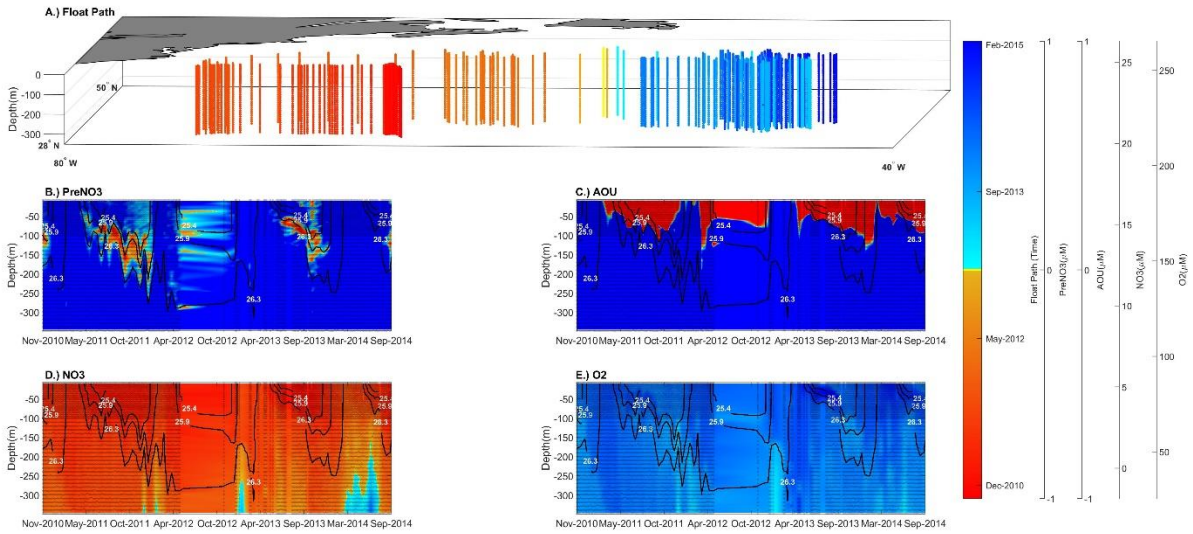

Figure S16. A.) Float path of Bermuda 6976 colored by time. B.) $PreNO_3$ for the first 350m of water column along float path Nov-10 to Feb-15, C.) AOU for the first 350m of water column along float path. D.) NO_3 for the first 350m of water column along float path. E.) O_2 for the first 350m of water column along float path. Black lines in B:E represent isopycnals,25.4$\frac{kg}{m^3}$, 25.9$\frac{kg}{m^3}$, and 26.3$\frac{kg}{m^3}$, chosen to outline anomalies. Dots in B:E represent observations. $PreNO_3$ and AOU limited to -1:1.

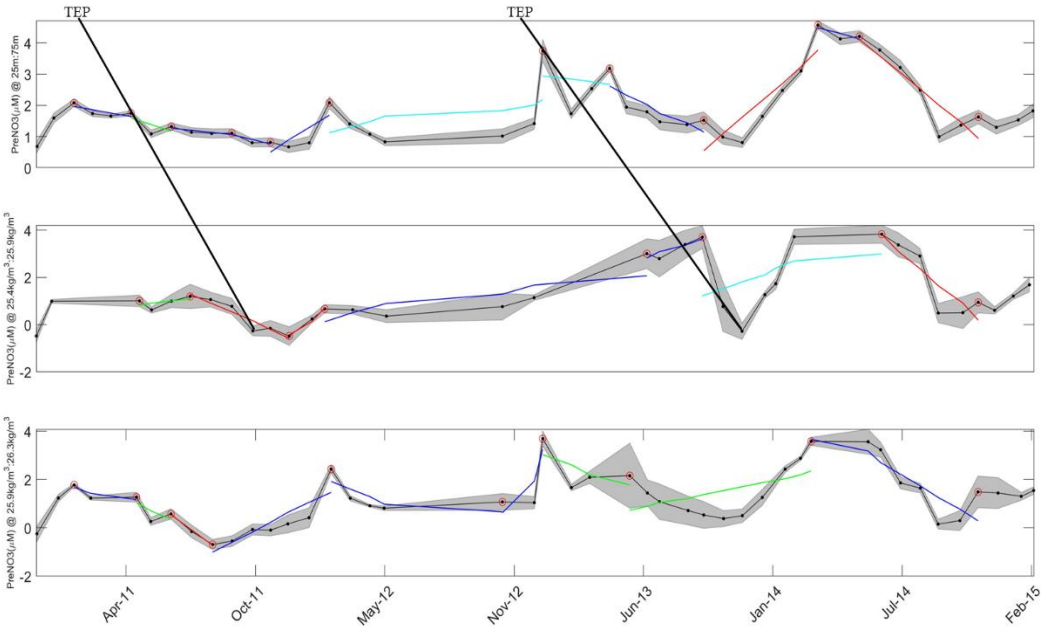

Figure S17. $PreNO_3$ for Bermuda 6976 smoothed to show $PreNO_3$ per month with regression of $PreNO_3$ vs time. Top figure PreNO3 at 25m-75m, middle figure $PreNO_3$ at 25.4 $\frac{kg}{m^3}$: 25.9$\frac{kg}{m^3}$, and bottom figure $PreNO_3$ at 25.9$\frac{kg}{m^3}$:26.3$\frac{kg}{m^3}$. Black dots are observations and the ones with red circles are local minima and maxima. Regressions colored by the value of the correlation coefficient; r^2>0.75(Red), 0.75> r^2>0.5(Blue), 0.5> r^2>0.25(Green), 0.25> r^2>0(Cyan). Grey regions represent 95% confidence intervals for $PreNO_3$ values. Black lines on figures indicate observations where TEP or VMP may have been responsible.

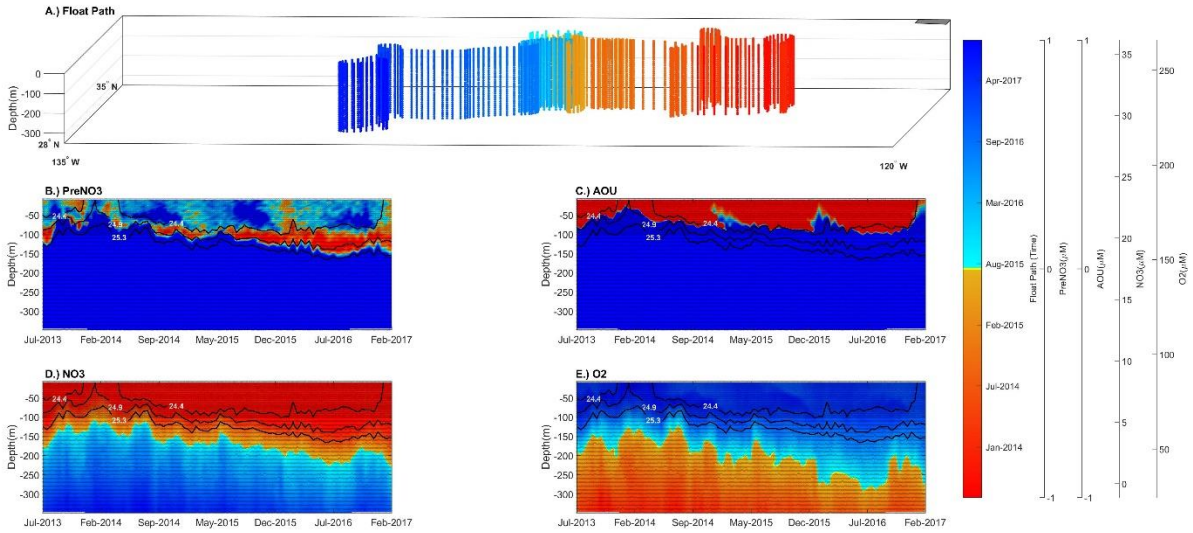

Figure S18. A.) Float path of CALCURRENT 7618 colored by time. B.) $PreNO_3$ for the first 350m of water column along float path from Jul-13 to Aug-17, C.) AOU for the first 350m of water column along float path. D.) NO_3 for the first 350m of water column along float path. E.) O_2 for the first 350m of water column along float path. Black lines in B:E represent isopycnals, 24$\frac{kg}{m^3}$, 24.5$\frac{kg}{m^3}$, and 25$\frac{kg}{m^3}$, chosen to outline anomalies. Dots in B:E represent observations. $PreNO_3$ and AOU limited to -1:1.

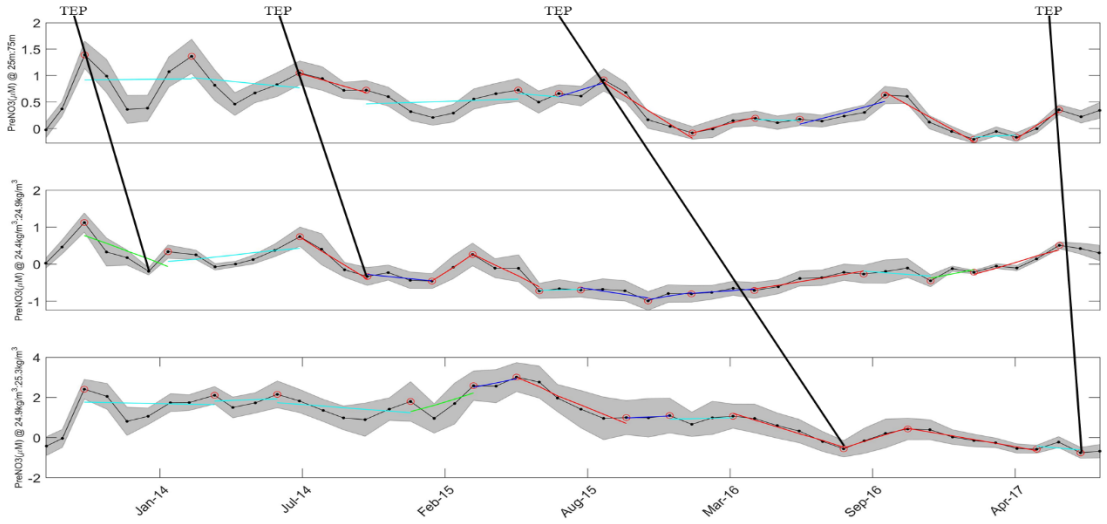

Figure S19. $PreNO_3$ for CALCURRENT 7618 smoothed to show $PreNO_3$ per month with regression of $PreNO_3$ vs time. Top figure $PreNO_3$ at 25m-75m, middle figure $PreNO_3$ at 24 $\frac{kg}{m^3}$: 24.5$\frac{kg}{m^3}$, and bottom figure $PreNO_3$ at 24.5$\frac{kg}{m^3}$:25$\frac{kg}{m^3}$. Black dots are observations and the ones with red circles are local minima and maxima. Regressions colored by the value of the correlation coefficient; r^2>0.75(Red), 0.75> r^2>0.5(Blue), 0.5> r^2>0.25(Green), 0.25> r^2>0(Cyan). Grey regions represent 95% confidence intervals for $PreNO_3$ values. Black lines on figures indicate observations where TEP or VMP may have been responsible.

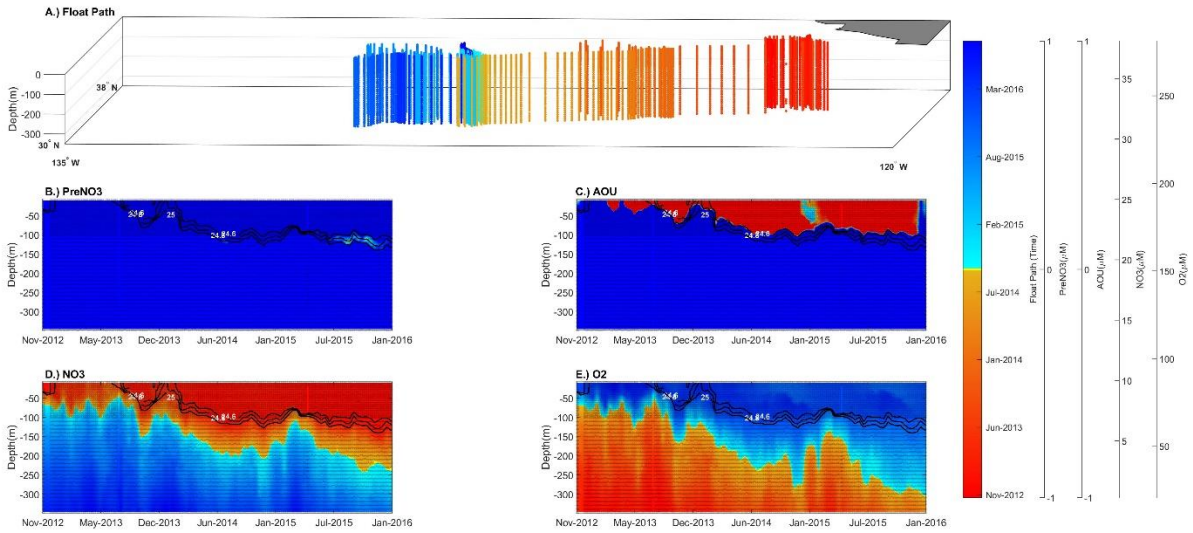

Figure S20. A.) Float path of CALCURRENT 7647 colored by time. B.) $PreNO_3$ for the first 350m of water column along float path from Nov-12 to Aug-16, C.) AOU for the first 350m of water column along float path. D.) NO_3 for the first 350m of water column along float path. E.) O_2 for the first 350m of water column along float path. Black lines in B:E represent isopycnals, 24.6$\frac{kg}{m^3}$, 24.8$\frac{kg}{m^3}$, and 25$\frac{kg}{m^3}$, chosen to outline anomalies. Dots in B:E represent observations. $PreNO_3$ and AOU limited to -1:1.

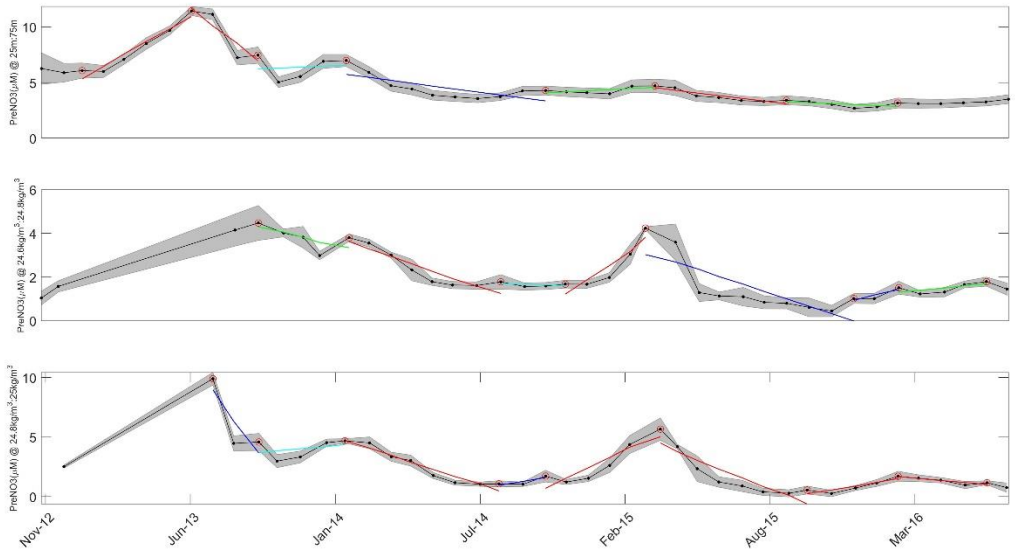

Figure S21. PreNO$_3$ for CALCURRENT 7647 smoothed to show PreNO$_3$ per month with regression of PreNO$_3$ vs time. Top figure PreNO$_3$ at 25m-75m, middle figure PreNO$_3$ at 24.6 $\frac{kg}{m^3}$: 24.8$\frac{kg}{m^3}$, and bottom figure PreNO$_3$ at 24.8$\frac{kg}{m^3}$:25$\frac{kg}{m^3}$. Black dots are observations and the ones with red circles are local minima and maxima. Regressions colored by the value of the correlation coefficient; r^2>0.75(Red), 0.75> r^2>0.5(Blue), 0.5> r^2>0.25(Green), 0.25> r^2>0(Cyan). Grey regions represent 95% confidence intervals for PreNO$_3$ values. Black lines on figures indicate observations where TEP or VMP may have been responsible.

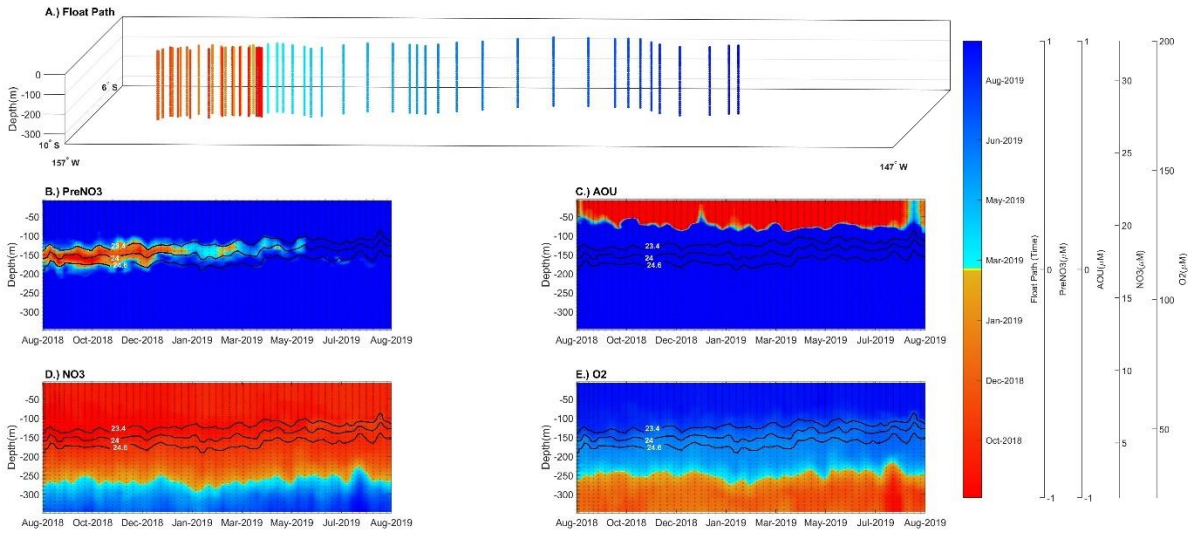

Figure S22. A.) Float path of EQPACW 8474 colored by time. B.) PreNO$_3$ for the first 350m of water column along float path from Aug-18 to Sep-19, C.) AOU for the first 350m of water column along float path. D.) NO$_3$ for the first 350m of water column along float path. E.) O$_2$ for the first 350m of water column along float path. Black lines in B:E represent isopycnals, 23.4$\frac{kg}{m^3}$, 24$\frac{kg}{m^3}$, and 24.6$\frac{kg}{m^3}$, chosen to outline anomalies. Dots in B:E represent observations. PreNO$_3$ and AOU limited to -1:1.

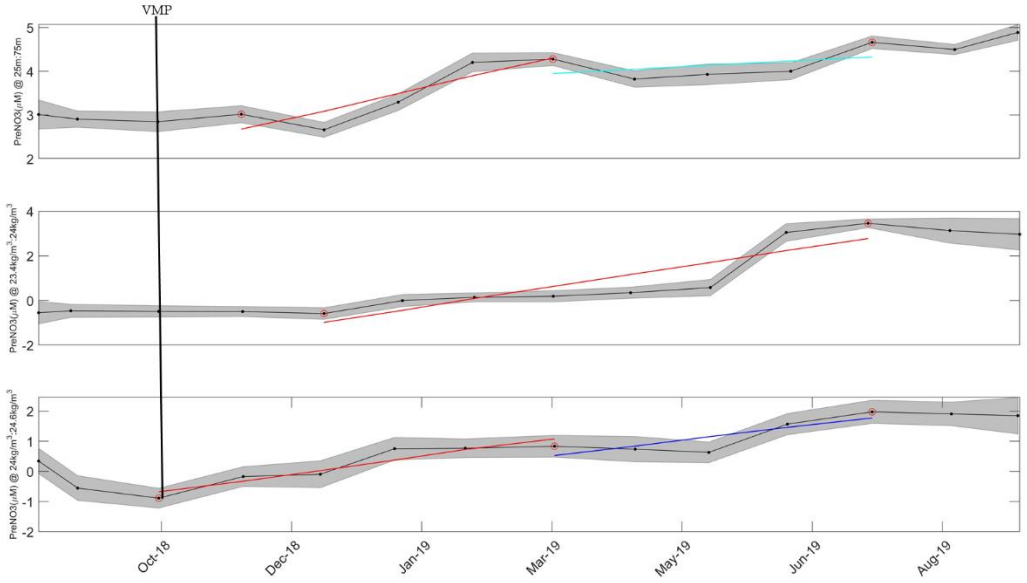

Figure S23. $PreNO_3$ for EQPACW 8474 smoothed to show $PreNO_3$ per month with regression of $PreNO_3$ vs time. Top figure PreNO3 at 25m-75m, middle figure $PreNO_3$ at 23.4$\frac{kg}{m^3}$: 24$\frac{kg}{m^3}$, and bottom figure $PreNO_3$ at 24$\frac{kg}{m^3}$:24.6$\frac{kg}{m^3}$. Black dots are observations and the ones with red circles are local minima and maxima. Regressions colored by the value of the correlation coefficient; r^2>0.75(Red), 0.75> r^2>0.5(Blue), 0.5> r^2>0.25(Green), 0.25> r^2>0(Cyan). Grey regions represent 95% confidence intervals for $PreNO_3$ values. Black lines on figures indicate observations where TEP or VMP may have been responsible.

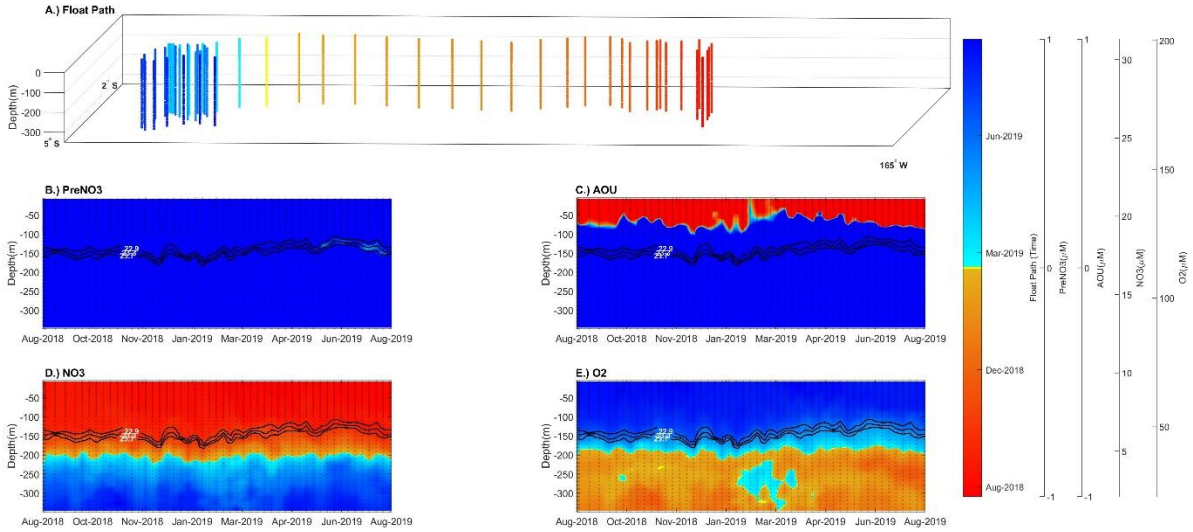

Figure S24. A.) Float path of EQPACW 12788 colored by time. B.) $PreNO_3$ for the first 350m of water column along float path from Aug-18 to Sep-19, C.) AOU for the first 350m of water column along float path. D.) NO_3 for the first 350m of water column along float path. E.) O_2 for the first 350m of water column along float path. Black lines in B:E represent isopycnals, 22.9$\frac{kg}{m^3}$, 23.3$\frac{kg}{m^3}$, and 23.7$\frac{kg}{m^3}$, chosen to outline anomalies. Dots in B:E represent observations. $PreNO_3$ and AOU limited to -1:1.

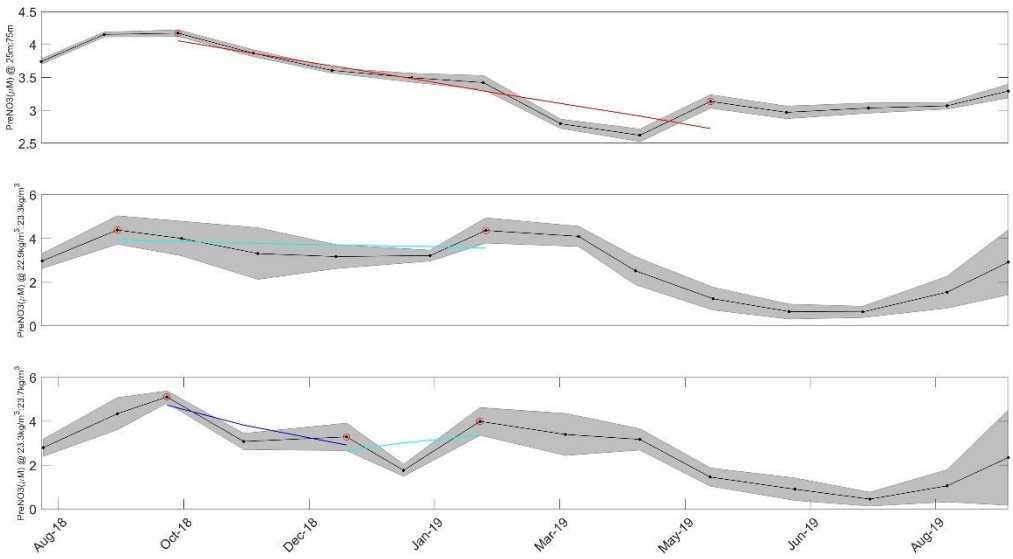

Figure S25. $PreNO_3$ for EQPACW 12788 smoothed to show $PreNO_3$ per month with regression of $PreNO_3$ vs time. Top figure PreNO3 at 25m-75m, middle figure $PreNO_3$ at 22.9$\frac{kg}{m^3}$: 23.3$\frac{kg}{m^3}$, and bottom figure $PreNO_3$ at 23.3$\frac{kg}{m^3}$:23.7$\frac{kg}{m^3}$. Black dots are observations and the ones with red circles are local minima and maxima. Regressions colored by the value of the correlation coefficient; r^2>0.75(Red), 0.75> r^2>0.5(Blue), 0.5> r^2>0.25(Green), 0.25> r^2>0(Cyan). Grey regions represent 95% confidence intervals for $PreNO_3$ values. Black lines on figures indicate observations where TEP or VMP may have been responsible.

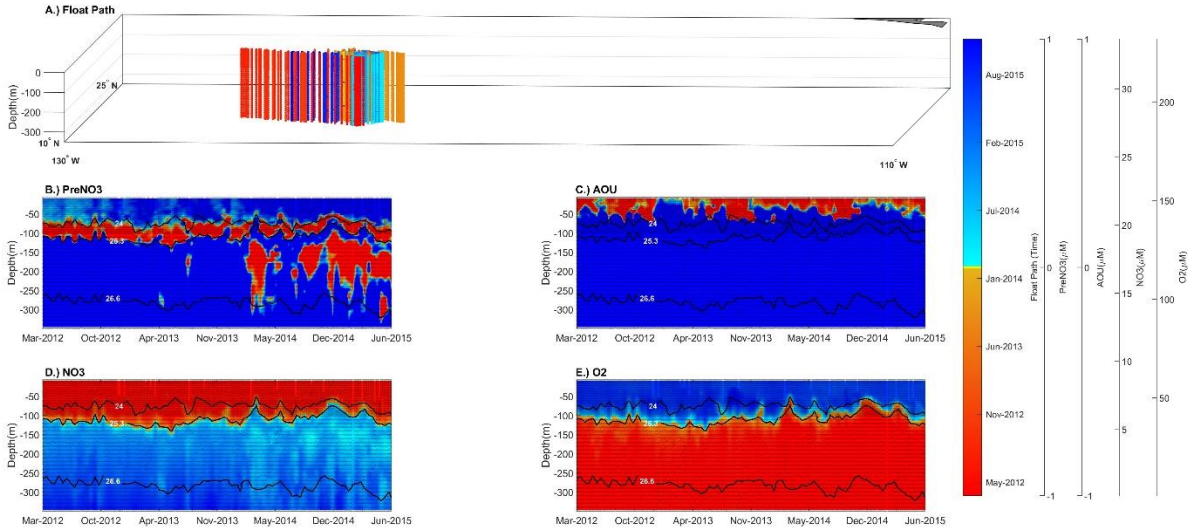

Figure S26. A.) Float path of ETNP 6960 colored by time. B.) $PreNO_3$ for the first 350m of water column along float path from Mar-12 to Dec-15, C.) AOU for the first 350m of water column along float path. D.) NO_3 for the first 350m of water column along float path. E.) O_2 for the first 350m of water column along float path. Black lines in B:E represent isopycnals, 24$\frac{kg}{m^3}$, 25.3$\frac{kg}{m^3}$, and 26.6$\frac{kg}{m^3}$, chosen to outline anomalies. Dots in B:E represent observations. $PreNO_3$ and AOU limited to -1:1.

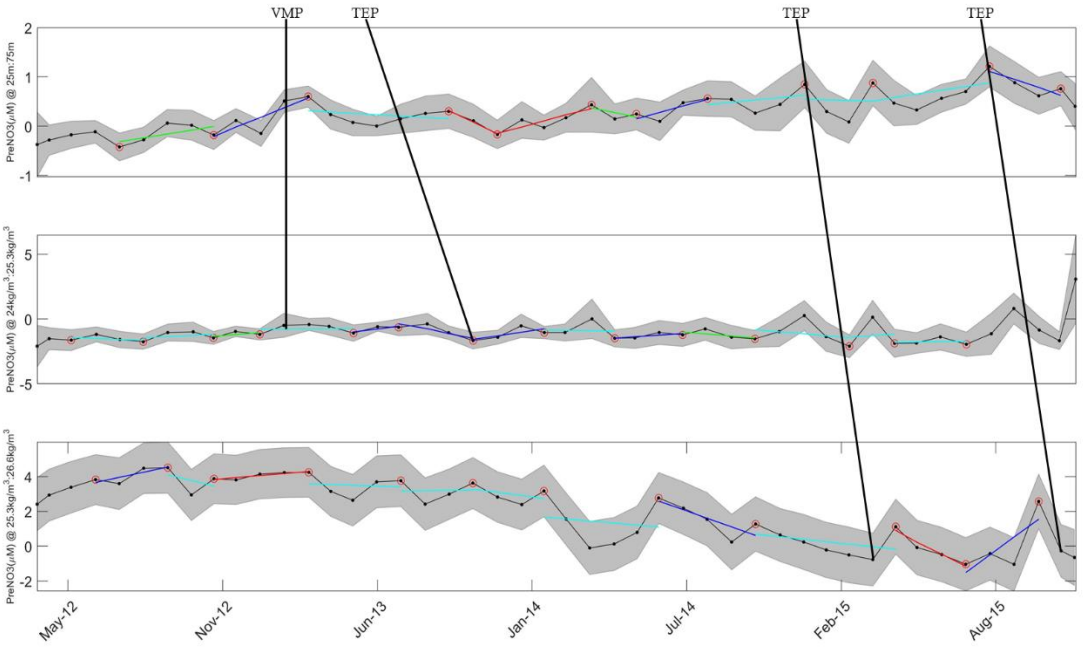

Figure S27. $PreNO_3$ for ETNP 6960 smoothed to show $PreNO_3$ per month with regression of $PreNO_3$ vs time. Top figure $PreNO_3$ at 25m-75m, middle figure $PreNO_3$ at $24\frac{kg}{m^3}$: $25.3\frac{kg}{m^3}$, and bottom figure $PreNO_3$ at $25.3\frac{kg}{m^3}$:$26.6\frac{kg}{m^3}$. Black dots are observations and the ones with red circles are local minima and maxima. Regressions colored by the value of the correlation coefficient; r^2>0.75(Red), 0.75> r^2>0.5(Blue), 0.5> r^2>0.25(Green), 0.25> r^2>0(Cyan). Grey regions represent 95% confidence intervals for $PreNO_3$ values. Black lines on figures indicate observations where TEP or VMP may have been responsible.

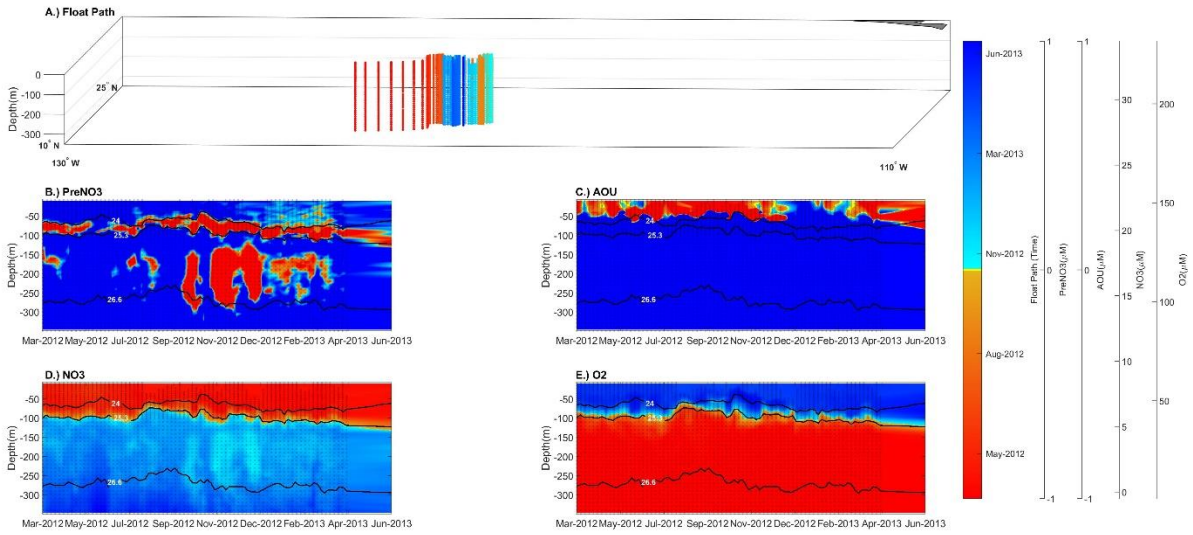

Figure S28. A.) Float path of ETNP 7558 colored by time. B.) $PreNO_3$ for the first 350m of water column along float path from Mar-12 to Jun-13, C.) AOU for the first 350m of water column along float path. D.) NO_3 for the first 350m of water column along float path. E.) O_2 for the first 350m of water column along float path. Black lines in B:E represent isopycnals, $24\frac{kg}{m^3}$, $25.3\frac{kg}{m^3}$, and $26.6\frac{kg}{m^3}$, chosen to outline anomalies. Dots in B:E represent observations. $PreNO_3$ and AOU limited to -1:1.

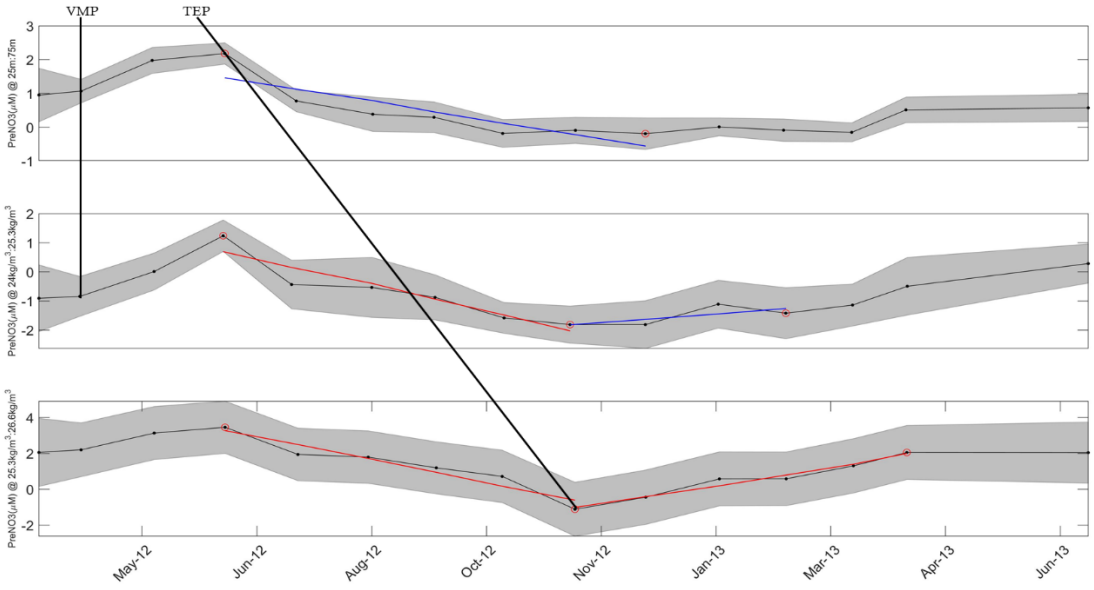

Figure S29. $PreNO_3$ for ETNP 7558 smoothed to show $PreNO_3$ per month with regression of $PreNO_3$ vs time. Top figure $PreNO_3$ at 25m-75m, middle figure $PreNO_3$ at $24\frac{kg}{m^3}$: $25.3\frac{kg}{m^3}$, and bottom figure $PreNO_3$ at $25.3\frac{kg}{m^3}$:$26.6\frac{kg}{m^3}$. Black dots are observations and the ones with red circles are local minima and maxima. Regressions colored by the value of the correlation coefficient; r^2>0.75(Red), 0.75> r^2>0.5(Blue), 0.5> r^2>0.25(Green), 0.25> r^2>0(Cyan). Grey regions represent 95% confidence intervals for $PreNO_3$ values. Black lines on figures indicate observations where TEP or VMP may have been responsible.

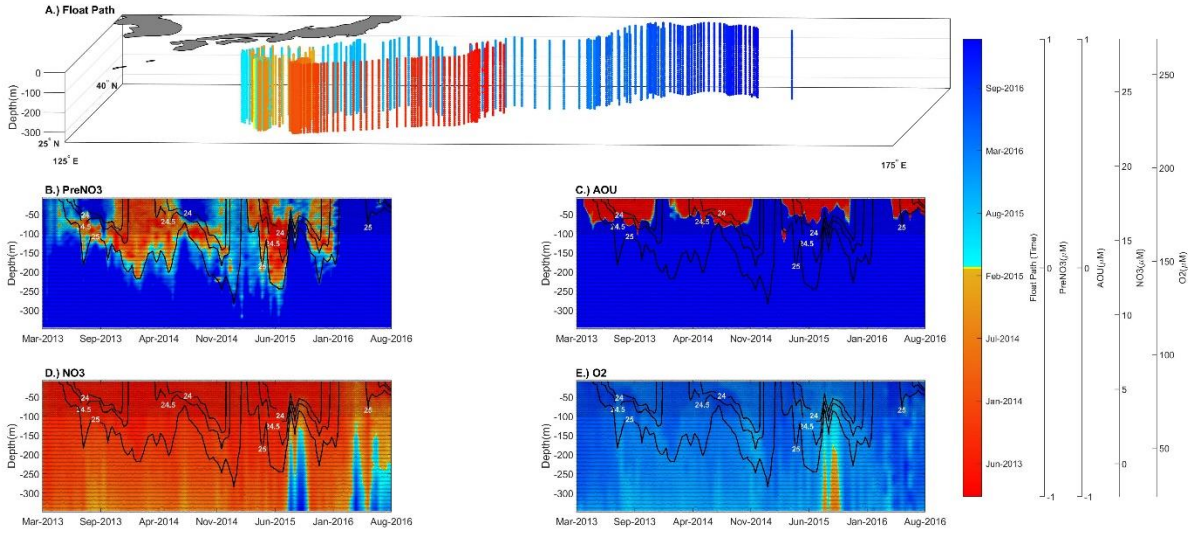

Figure S30. A.) Float path of KUROSHIO 7546 colored by time. B.) $PreNO_3$ for the first 350m of water column along float path from Mar-13 to Mar-17, C.) AOU for the first 350m of water column along float path. D.) NO_3 for the first 350m of water column along float path. E.) O_2 for the first 350m of water column along float path. Black lines in B:E represent isopycnals $24\frac{kg}{m^3}$, $24.5\frac{kg}{m^3}$, and $25\frac{kg}{m^3}$, chosen to outline anomalies. Dots in B:E represent observations. $PreNO_3$ and AOU limited to -1:1.

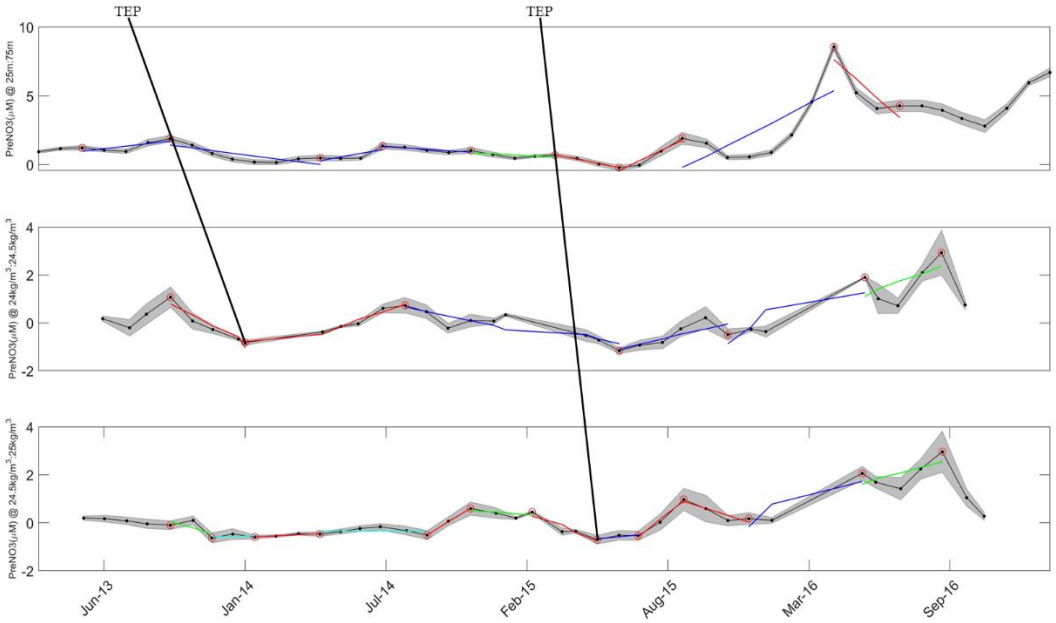

Figure S31. $PreNO_3$ for KUROSHIO 7546 smoothed to show $PreNO_3$ per month with regression of $PreNO_3$ vs time. Top figure $PreNO_3$ at 25m-75m, middle figure $PreNO_3$ at $24\frac{kg}{m^3}$: $24.5\frac{kg}{m^3}$, and bottom figure $PreNO_3$ at $24.5\frac{kg}{m^3}$:$25\frac{kg}{m^3}$. Black dots are observations and the ones with red circles are local minima and maxima. Regressions colored by the value of the correlation coefficient; r^2>0.75(Red), 0.75> r^2>0.5(Blue), 0.5> r^2>0.25(Green), 0.25> r^2>0(Cyan). Grey regions represent 95% confidence intervals for $PreNO_3$ values. Black lines on figures indicate observations where TEP or VMP may have been responsible.

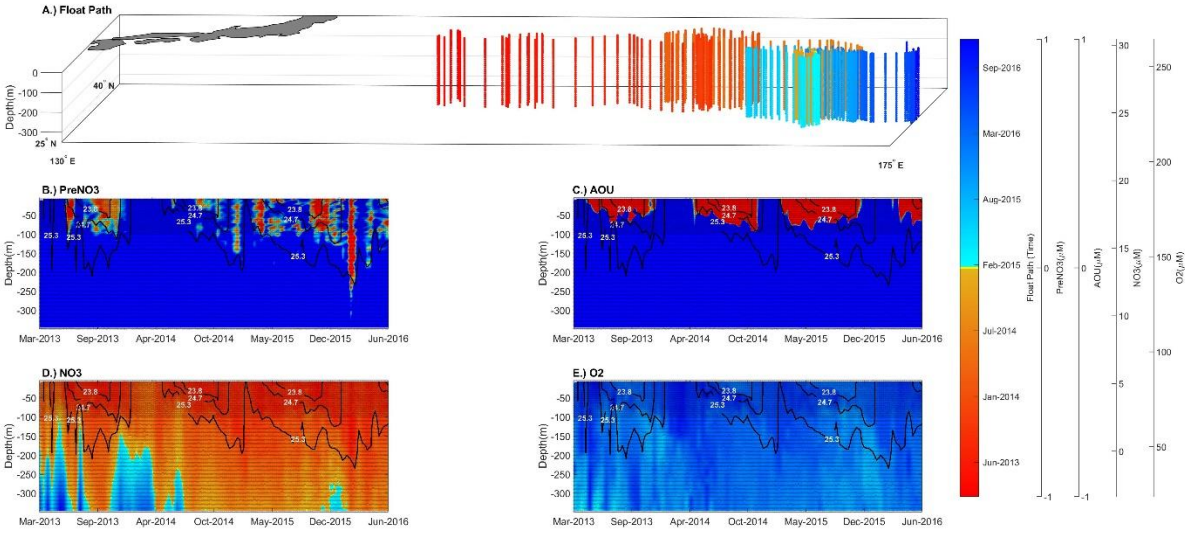

Figure S32. A.) Float path of KUROSHIO 7674 colored by time. B.) $PreNO_3$ for the first 350m of water column along float path from Mar-13 to Jan-17, C.) AOU for the first 350m of water column along float path. D.) NO_3 for the first 350m of water column along float path. E.) O_2 for the first 350m of water column along float path. Black lines in B:E represent isopycnals $23.8\frac{kg}{m^3}$, $24.7\frac{kg}{m^3}$, and $25.3\frac{kg}{m^3}$, chosen to outline anomalies. Dots in B:E represent observations. $PreNO_3$ and AOU limited to -1:1.

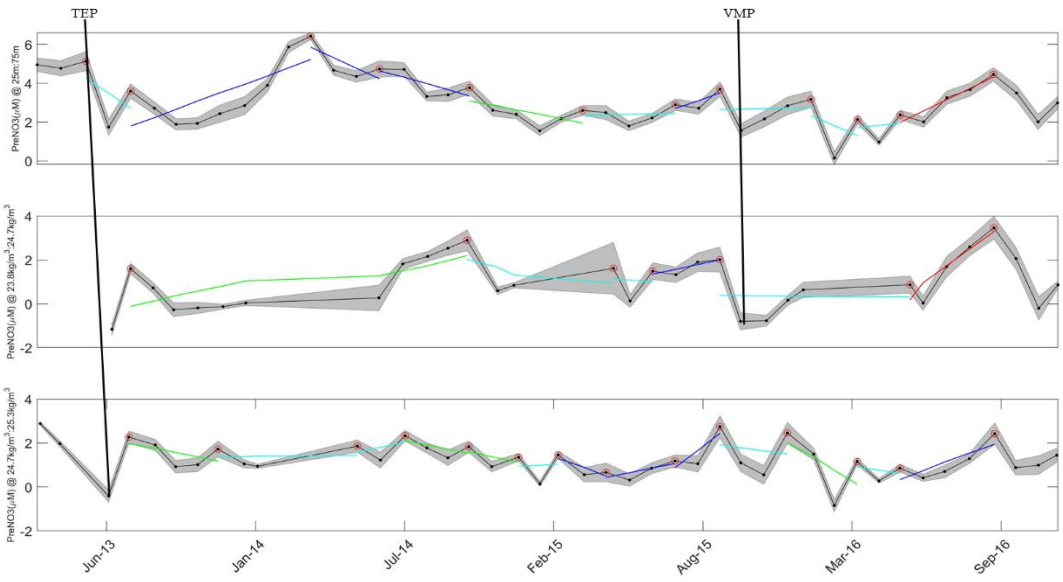

Figure S33. $PreNO_3$ for KUROSHIO 7674 smoothed to show $PreNO_3$ per month with regression of $PreNO_3$ vs time. Top figure $PreNO_3$ at 25m-75m, middle figure $PreNO_3$ at 23.8$\frac{kg}{m^3}$: 24.7$\frac{kg}{m^3}$, and bottom figure $PreNO_3$ at 24.7$\frac{kg}{m^3}$:25.3$\frac{kg}{m^3}$. Black dots are observations and the ones with red circles are local minima and maxima. Regressions colored by the value of the correlation coefficient; r^2>0.75(Red), 0.75> r^2>0.5(Blue), 0.5> r^2>0.25(Green), 0.25> r^2>0(Cyan). Grey regions represent 95% confidence intervals for $PreNO_3$ values. Black lines on figures indicate observations where TEP or VMP may have been responsible.

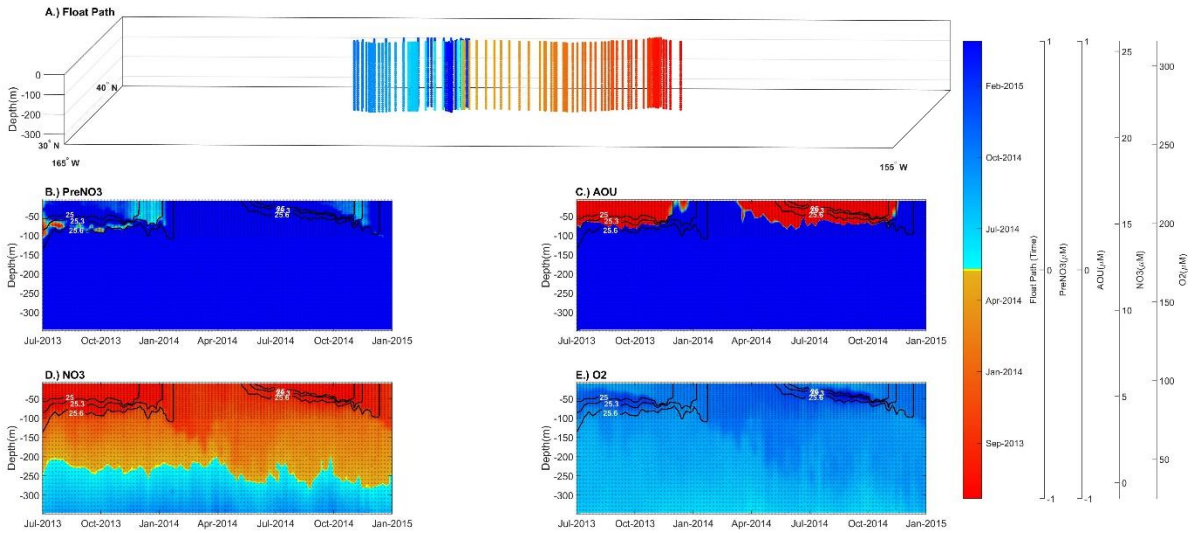

Figure S34. A.) Float path of NOPACIFIC 7642 colored by time. B.) $PreNO_3$ for the first 350m of water column along float path from Jul-13 to Apr-15, C.) AOU for the first 350m of water column along float path. D.) NO_3 for the first 350m of water column along float path. E.) O_2 for the first 350m of water column along float path. Black lines in B:E represent isopycnals 25$\frac{kg}{m^3}$, 25.3$\frac{kg}{m^3}$, and 25.6$\frac{kg}{m^3}$, chosen to outline anomalies. Dots in B:E represent observations. $PreNO_3$ and AOU limited to -1:1.

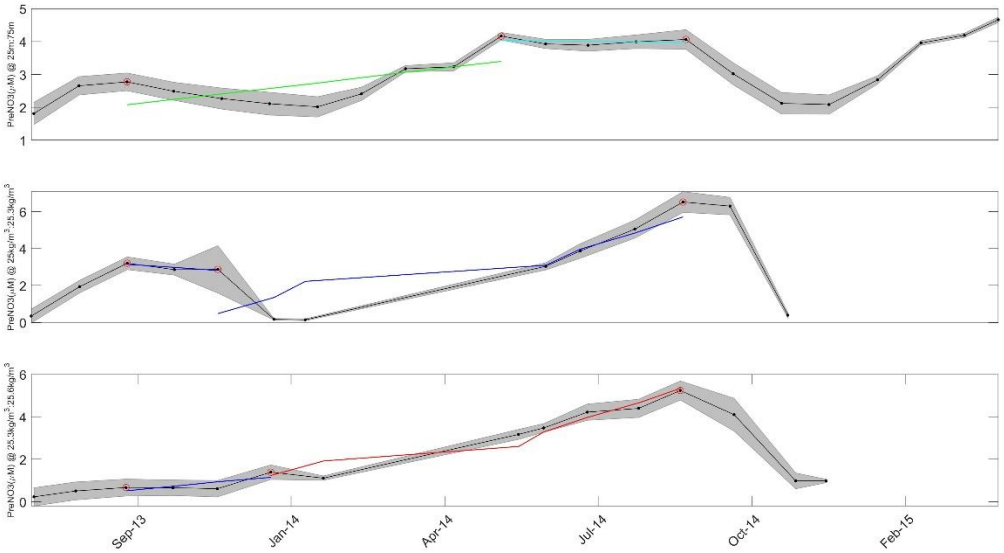

Figure S35. $PreNO_3$ for NOPACIFIC 7642 smoothed to show $PreNO_3$ per month with regression of $PreNO_3$ vs time. Top figure PreNO3 at 25m-75m, middle figure $PreNO_3$ at 25$\frac{kg}{m^3}$: 25.3$\frac{kg}{m^3}$, and bottom figure $PreNO_3$ at 25.3$\frac{kg}{m^3}$:25.6$\frac{kg}{m^3}$. Black dots are observations and the ones with red circles are local minima and maxima. Regressions colored by the value of the correlation coefficient; r^2>0.75(Red), 0.75> r^2>0.5(Blue), 0.5> r^2>0.25(Green), 0.25> r^2>0(Cyan). Grey regions represent 95% confidence intervals for $PreNO_3$ values. Black lines on figures indicate observations where TEP or VMP may have been responsible.

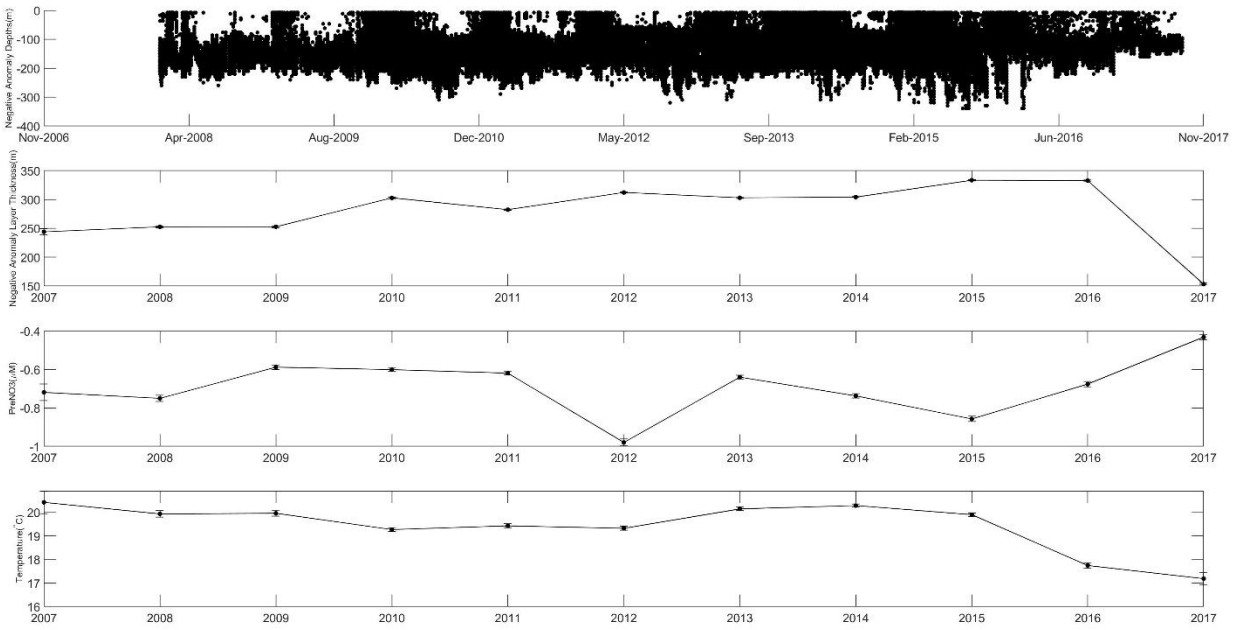

Figure S36. Interannual Variability of North Pacific; depths where negative $PreNO_3$ occurred (Top Panel), Thickness of layer were negative $PreNO_3$ occurred smoothed by year (Second Panel), $PreNO_3$ from the negative $PreNO_3$ layer smoothed by year (Third Panel), Temperature smoothed by year (Bottom Panel). Error bars are standard error.